



## Deliverable D4.1.4 – Validation of innovations by tests on component level

Agreement n.:	308974
Duration	November 2012 – October 2017
Co-ordinator:	Danmarks Tekniske Universitet
Supported by:	



The research leading to these results has received funding from the European Community's Seventh Framework Programme FP7-ENERGY-2012-1-2STAGE under grant agreement No. 308974 (INNWIND.EU).

---

#### PROPRIETARY RIGHTS STATEMENT

This document contains information, which is proprietary to the "INNWIND.EU" Consortium. Neither this document nor the information contained herein shall be used, duplicated or communicated by any means to any third party, in whole or in parts, except with prior written consent of the "INNWIND.EU" consortium.

---

# Document information

<b>Document Name:</b>	Deliverable D4.1.4. – Validation of innovations by tests on component level
<b>Confidentiality Class</b>	Public
<b>Document Number:</b>	Deliverable D 4.1.4
<b>Author:</b>	Niklas Scholle, Luka Radulović (LUH) Rogier Nijssen, Francisco Lahuerta (WMC) Lars Bo Ibsen (AAU) Martin Kohlmeier, Aligi Foglia (FhG-H)
<b>Review:</b>	Aligi Foglia, Martin Kohlmeier
<b>Date:</b>	2015-11-09
<b>WP:</b>	4 Offshore Foundations and Support Structures
<b>Task:</b>	4.1 Innovations on component level for bottom-based structures

## 1 TABLE OF CONTENTS

<b>1</b>	<b>Table of contents .....</b>	<b>3</b>
<b>2</b>	<b>Introduction.....</b>	<b>4</b>
	References.....	4
<b>3</b>	<b>INNOVATIVE MATERIALS.....</b>	<b>5</b>
3.1	Sandwich material for tubes.....	5
3.1.1	Test specimen preparation .....	6
3.1.2	Experimental setup .....	7
3.1.3	Experimental results .....	8
3.1.4	Conclusion .....	14
3.2	Sandwich material for connections and joints .....	15
3.2.1	Experimental programme on subcomponent – Joint test design.....	15
3.2.2	Experimental test results .....	21
3.2.3	Conclusions and recommendations.....	23
	References .....	24
<b>4</b>	<b>SOIL &amp; FOUNDATION .....</b>	<b>25</b>
4.1	Suction bucket foundations.....	25
4.1.1	Experimental Details .....	26
4.1.2	Experimental test program .....	29
4.1.3	Results .....	32
4.1.4	Tensile cyclic loadings with different overburden pressure.....	33
4.1.5	Loading rate effect from two-way loading in tension and compression.....	39
4.1.6	Observation on stiffness behaviour under vertical cyclic loading .....	39
4.1.7	Conclusions and recommendations.....	42
4.2	Soil pile interaction / axial pile loading.....	43
4.2.1	Description of testing facility and material .....	43
	Preparation of the sand sample .....	44
	Property of the piles .....	45
4.2.2	Assessment of the sand sample properties .....	45
	Soil core sampling .....	46
	Dynamic probe light and cone penetration test .....	46
	Soil properties after the installation of Pile 1 .....	48
4.2.3	Test phases.....	50
	Instrumentation of the piles.....	50
	Installation of the piles.....	51
	Pre-loading phase.....	52
	Tensile loading test .....	52
4.2.4	Example results .....	53
	References.....	54
<b>5</b>	<b>Conclusions.....</b>	<b>55</b>

## 2 INTRODUCTION

As reported in [2-01] reducing the levelised cost of energy (LCOE) is the key factor towards a sustainable development of offshore wind energy source. Optimizing the design of support structures for offshore wind turbines is paramount to the reduction of the LCOE. To enhance the technology readiness level (TRL) and eventually bring cost-effective innovations to the offshore wind industry, new technologies must be tested in realistic environments under appropriate load situations. Moreover, new innovations cannot only refer to one specific sub-component and the synergy between different expertise becomes strategic. In this deliverable, experimental campaigns addressing the potential development of new technologies for offshore wind sub-structures are reported.

The scientific content of this document consists of two chapters, the first regarding innovative material for jacket structures (Chapter 2) and the second regarding soil-foundation interaction (Chapter 3). In these two chapters four experimental campaigns are described. Test aims, experimental setups, test phases and example results are included.

In Chapter 2 sandwich material for tubes and joints are tested. The braces of jackets are normally constructed with steel. Instead of using standard steel tubes, ultra-high performance concrete might be used between inner and outer tubes to save material and thereby weight. The main disadvantage of this material is its brittle behavior. The tests presented explore the response of this sandwich material subjected to combined moment and axial loading. Sandwich material for joints and connections are also investigated. It is stressed that sandwich tubular constructions enhance the structural efficiency of the element increasing the buckling load. As a result of that fatigue becomes the predominant design driver. Both static and fatigue tests were performed with the aim to evaluate the joint behavior. The specimen consisted of a symmetric metal-cement sandwich brace which was placed in the testing machine and gripped at lower and upper base by means of resin. The 1 MN capacity testing machine applied axial static or dynamic load in tension to the specimen.

In Chapter 3 bucket foundations and vibro-driven piles are investigated as potential cost-saving technologies for offshore wind turbine foundations. Both the evaluated technologies could potentially be cost-effective as a consequence of the advantages presented by the installation methods. Nevertheless, the bearing behavior of bucket foundations and vibro-driven piles has not been extensively investigated and yet this is necessary to prove the cost-saving potential of these foundations. The experimental campaign concerning bucket foundations consists of a number of static and cyclic tests aiming at disclosing some general behavioral patterns of this foundation under axial loading. The sub-chapter dedicated to vibro-driven piles presents details about the geotechnical sand pit preparation and about the various investigations performed in order to extrapolate the soil parameters. Moreover, information on the soil after the pile installation is reported.

In deliverable [2-02] the experimental results herein presented will be interpreted in order to validate novel design methods.

### References

- [2-01] INN WIND.EU: Innovations on component level (interim report). Deliverable 4.1.2, 2015.
- [2-02] INN WIND.EU: Innovations on component level (final report). Deliverable 4.1.3, 2015.

### 3 INNOVATIVE MATERIALS

Authors: Radulovic, Luka; Scholle, Niklas (Leibniz Universität Hannover - LUH)  
Nijssen, Rogie; Lahuerta, Francisco (Knowledge Centre Wind turbine Materials and Constructions - WMC)

#### 3.1 Sandwich material for tubes

Sandwich tubes are rod-like structural components consisting of three components: two relatively thin steel tubes and a core made of ultra-high performance concrete (UHPC). Figure 3.1-1 shows the top view of a sandwich component. Due to its high strength, UHPC is an appropriate alternative to save material and weight. However, feasible construction methods for UHPC must consider material specific features. A compressive strength almost comparable to that of construction steel is one of the specific features of this rather new building material. Another key feature of UHPC is its brittle failure behaviour. For practical application of UHPC, it is essential to gain control of this unfavorable failure behaviour through appropriate construction methods. The sandwich tube concept is such an approach for materials-oriented ductile design with UHPC.

In consideration of the operation area as a strut component of a jacket structure the loading situation for the sandwich tube components is particularly characterized by the combination of moments and axial forces [3-01].

The structural behavior of this load combination shall be investigated in the following chapter. The evaluation of bending and axial load interaction is based on eccentric compression tests.

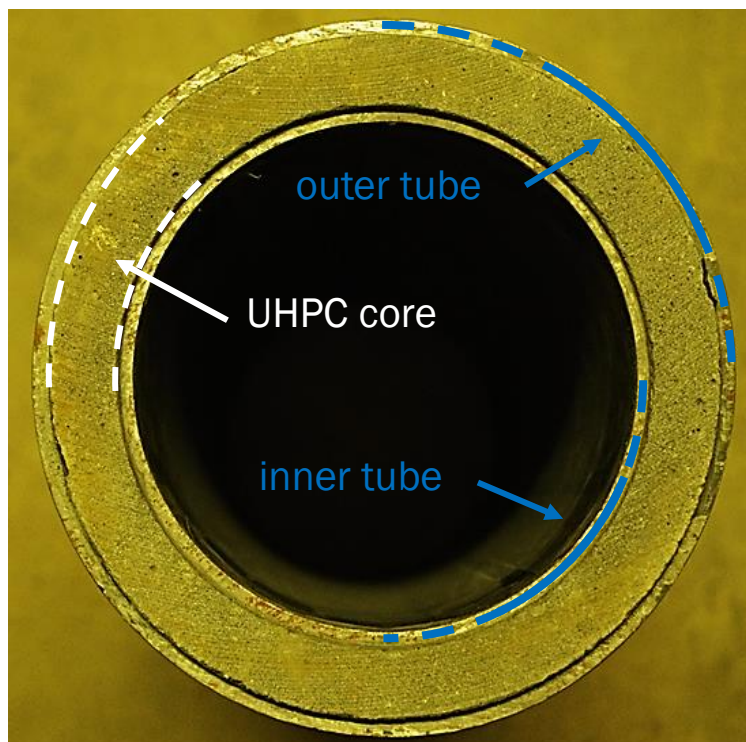


Figure 3.1-1 – Top view of a sandwich component cross section.

### 3.1.1 Test specimen preparation

**Table 3.1-1 – Geometrical dimensions of tested specimen.**

Component	Outer diameter	Thickness	Cross section area
	[mm]	[mm]	[mm <sup>2</sup> ]
Outer Tube	177.80	4.50	2449.97
UHPC core	168.80	19.90	9308.88
inner Tube	133.00	4.00	1621.06

The geometrical dimensions of the tested sandwich components are shown in Table 3.1-1. The steel tubes consist of steel grade P235.



**Figure 3.1-2 – Specimen preparation – concentrically aligned steel tubes (left) and filling of core material (right).**

Impressions of the test specimen preparation are shown in Figure 3.1-2. The left picture shows three sandwich tubes before filling. Inner and outer steel tubes are aligned concentrically with each other and are fixed by self-made clamping devices. The right picture shows the filling process of the sandwich tubes. The UHPC core material is pumped into the gap between the inner and outer steel tubes by a spiral pump. To quantify material properties additional samples of material are produced. In order to unify the curing of the core material, the hybrid tubes are subjected to a 48-hour lasting heat treatment after demolding.

**Table 3.1-2 – UHPC material properties.**

UHPC material properties		Unit	mean value	standard deviation
Compression strength (100mm cube)	$f_c$	[N/mm <sup>2</sup> ]	207.97	11.23
Flexural strength (40x40x160mm beam)	$f_{cb}$	[N/mm <sup>2</sup> ]	16.64	1.24
Density	P	[kg/m <sup>3</sup> ]	2333.82	15.28

Table 3.1-2 reveals the determined material properties by the mean value as well as the standard deviation of the used UHPC core material.

To exclude local failure at the head or bottom of the tubular structure the ends of the specimens are poured into so-called load plates. As grout material the same UHPC material is used. After casting the load plates, the specimens are subjected to an additional heat treatment.

### 3.1.2 Experimental setup

An eccentric loading test setup was developed. The bearing conditions with two line joints generates a reproducible load situation. Furthermore, the reusable test setup allows the attachment of measuring applications at defined locations. Thus, creating a possibility of direct comparison of the measured test results.

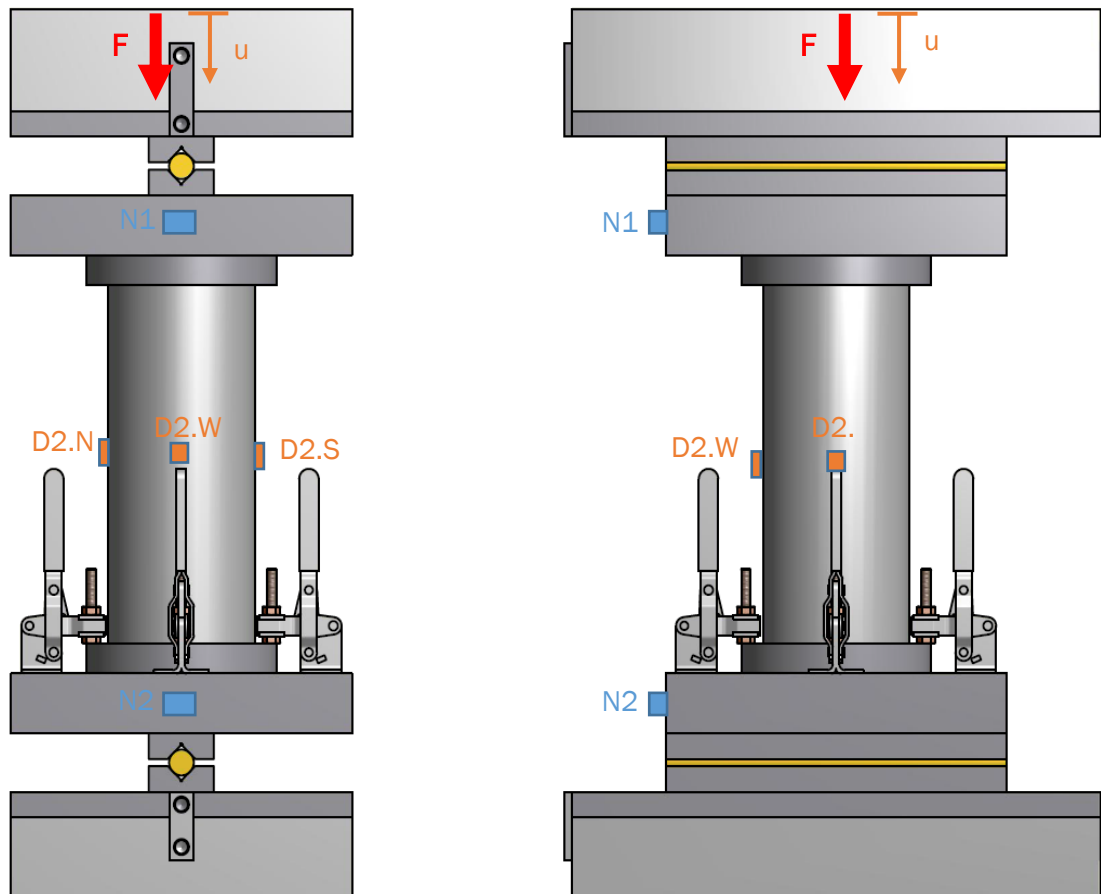


Figure 3.1-3 – Measurement setup.

Figure 3.1-3 shows the measurement setup. The following values are detected at a measuring rate of 50 Hz:

- compression load (F)
- deflection (u)
- top (N1) and bottom (N2) inclination
- vertical and horizontal steel strain at the center of the sample respectively in the compression (D2.N), tension (D2.S) and neutral (D2.W) axis

Table 3.1-3 – Experimental settings.

Specimen label	Eccentricity	Eccentricity ratio	Loading speed
	[mm]	[-]	[mm/min]
SC-0-1	0.00	0.00	0.10
SC-0-2	0.00	0.00	0.30
SC-0-3	0.00	0.00	0.30
SC-1-1	28.50	0.16	0.30

SC-1-2	28.50	0.16	0.30
SC-1-3	28.50	0.16	0.30
SC-2-1	57.00	0.32	0.30
SC-2-2	57.00	0.32	0.30
SC-2-3	57.00	0.32	0.30

Experimental settings of the tested sandwich components are listed in Table 3.1-3. The eccentricity ratio is the relation between eccentricity and outer diameter of the specimen.



Figure 3.1-4 – Test setup.

Figure 3.1-4 shows a test specimen installed in the test setup. The experiments were carried out with a servo-hydraulic 5MN-compression testing rig. The load was applied displacement-controlled at a test speed of 0.3 mm/min. An exception is sample SC-0-1, the test speed was set to be only 0.1 mm/min for the first test due to safety issues.

### 3.1.3 Experimental results

Figure 3.1-5 shows the resulting load bearing behaviour of sandwich tubes under static centric loading conditions. The abscissa illustrates the compression load and the ordinate visualizes the measured deflection.

The curve progression can be classified by three characteristics: First characteristic is a nearly linear increase completed by reaching the ultimate bearing capacity. Second characteristic is a subsequent reduction of bearing capacity. Final characteristic is a residual load bearing level. The results of the experiments confirm the findings from *Lindschulte* in [3-02] for static centric loaded sandwich tubes.

The lower gradient of the load-displacement curve of the sample SC-0-1 in Figure 3.1-5 can be explained by its lower loading speed.

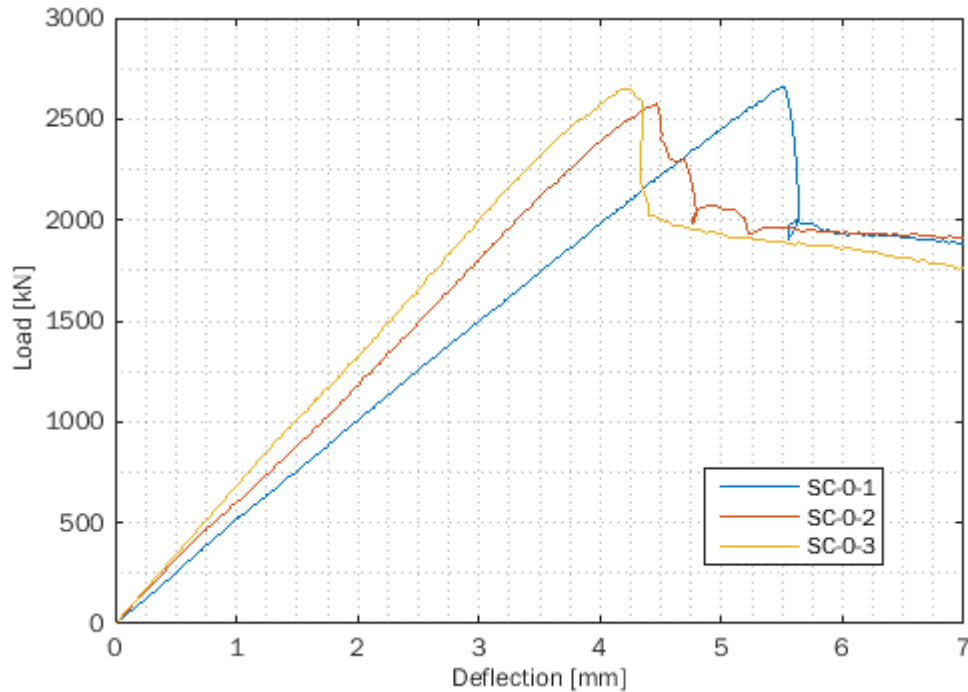


Figure 3.1-5 – Load-Deflection ( $e = 0$ ).

Figure 3.1-6 visualizes exemplarily vertical strain gauge measurement data of representative test Specimen SC-0-3. The vertical deformation spreads evenly over the circumferential annulus until about 60% of the maximum load. From then on the vertical compression in the pressure axis increases disproportionately. After reaching maximum capacity stresses redistributes within the annulus cross section.

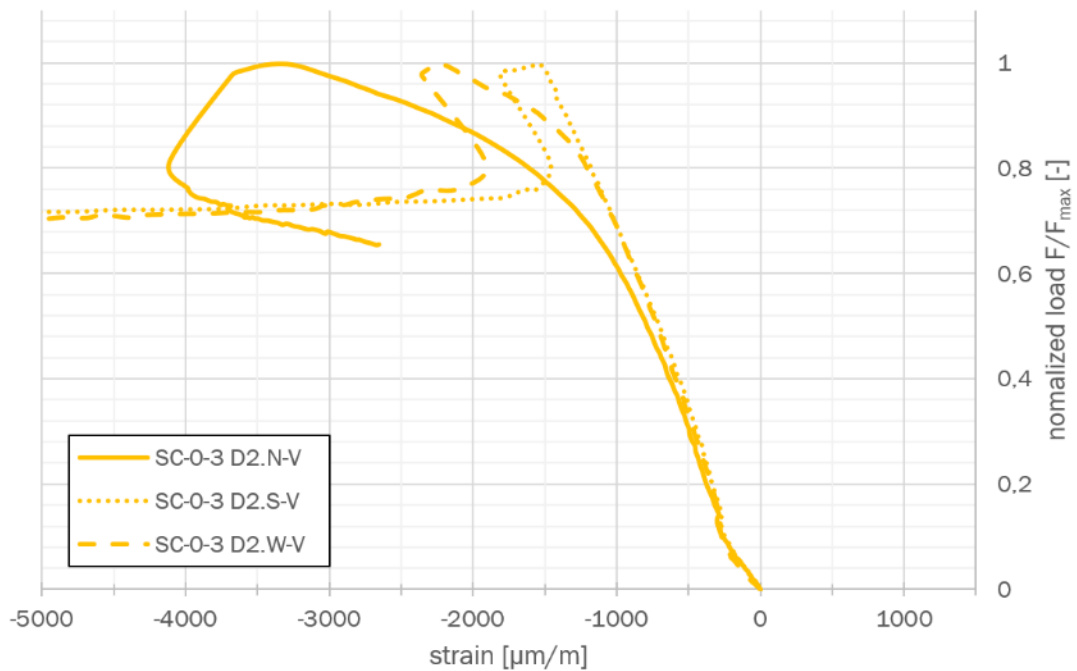


Figure 3.1-6 – Strain gauge evolution of SC-0-3.

Figure 3.1-7 shows load deflection development of test specimens at eccentricity level  $e = 28.5$  mm. The qualitative and quantitative similarity of the load-displacement curves indicates a good reproducibility of the test results.

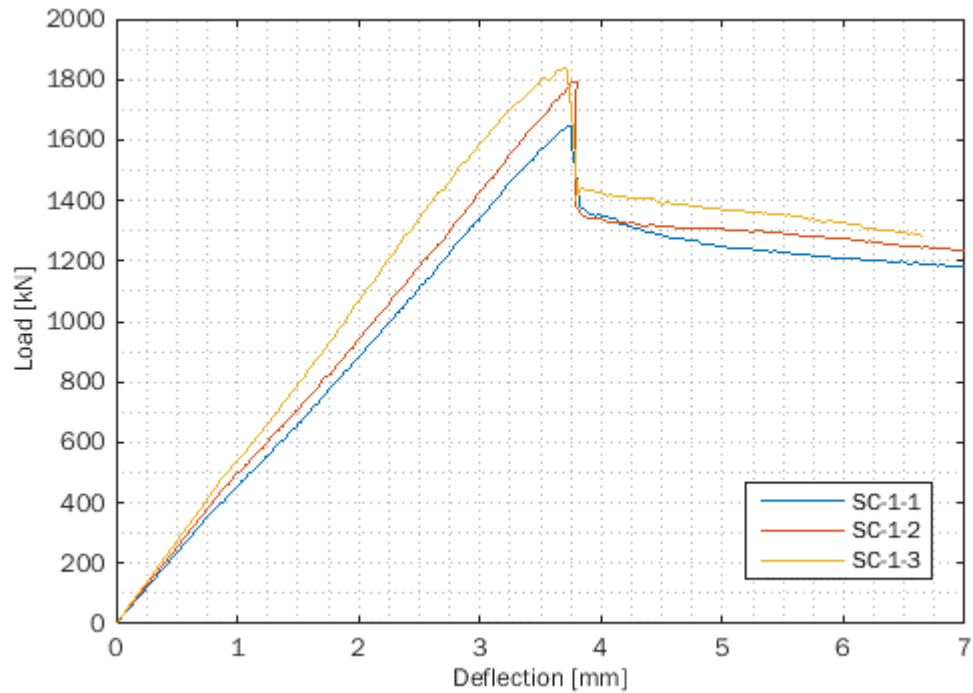


Figure 3.1-7 – Load-Deflection ( $e = 28.5$  mm).

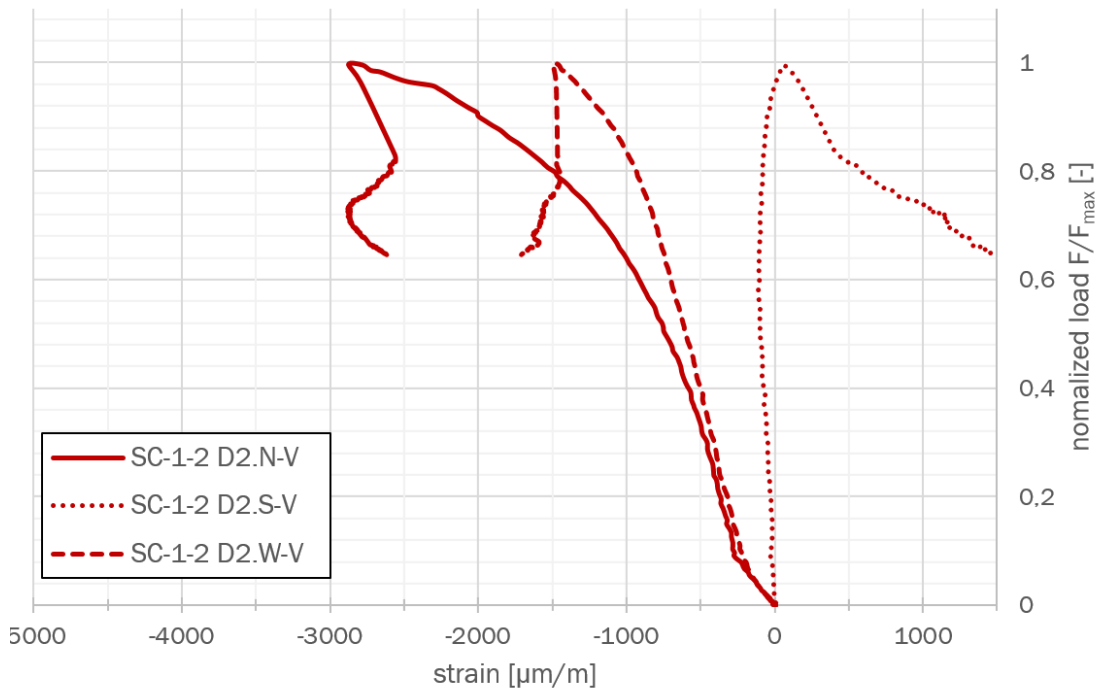


Figure 3.1-8 – Strain gauge evolution of SC-1-2.

Figure 3.1-8 shows strain gauge measurement data of representative test Specimen SC-1-2. The contrast to centric load condition (see Figure 3.1-6) can be seen clearly. The unevenness of the

stress distribution in the cross section gets more pronounced with increasing load. Nevertheless, compression prevails even in the tension axis.

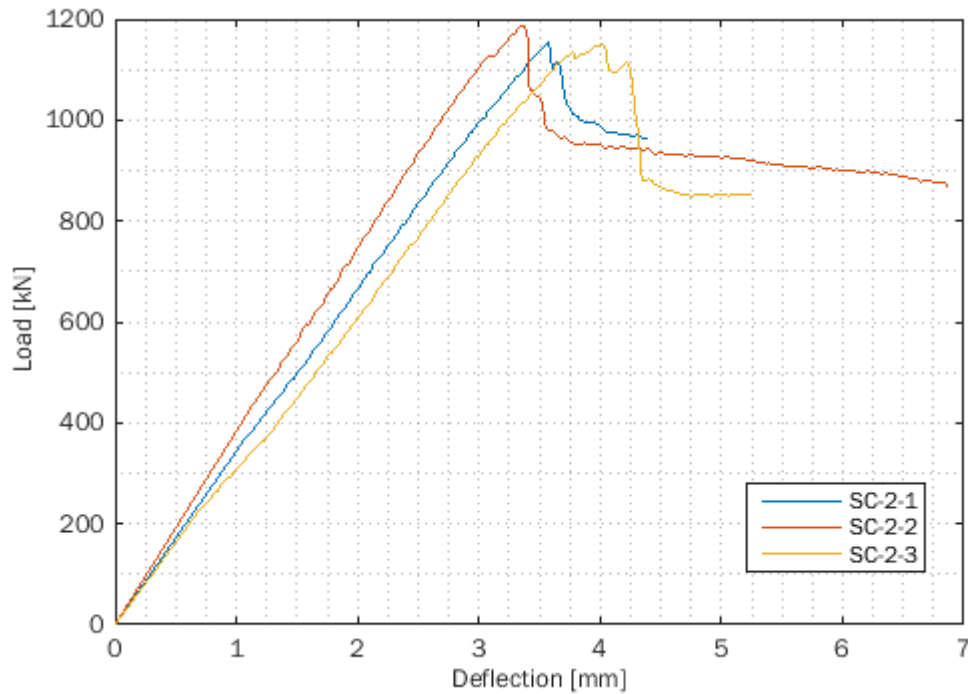


Figure 3.1-9 – Load-Deflection ( $e = 57.0$  mm).

Figure 3.1-9 shows the development of the load deflection curve of test specimens at eccentricity  $e = 57.0$  mm. As in the previous experiments, a comparatively small scattering of the repeated tests is observed.

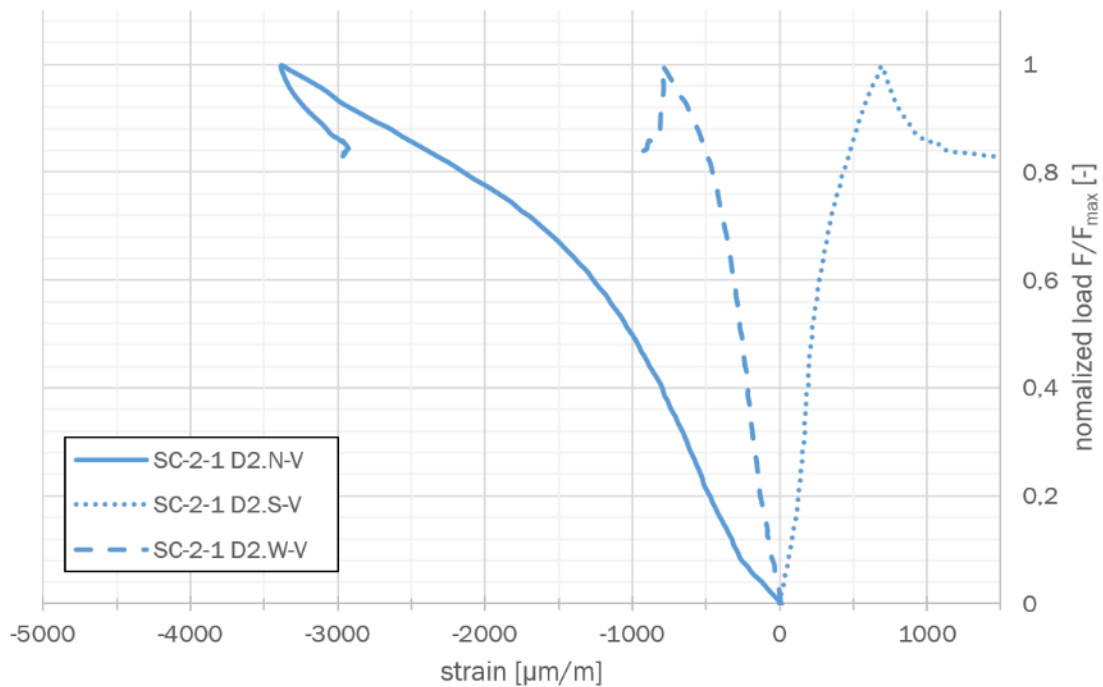


Figure 3.1-10 – Strain gauge evolution of SC-2-1.

Figure 3.1-10 visualizes strain gauge measurement data of representative test Specimen SC-2-1. The increasing differentiation of the strain gradients within the circular cross section is clearly visible. The eccentric load introduction at an eccentricity of  $e = 57.0$  mm leads to tensile strain in the tension axis. The cross-section is no longer in a completely compressed state.

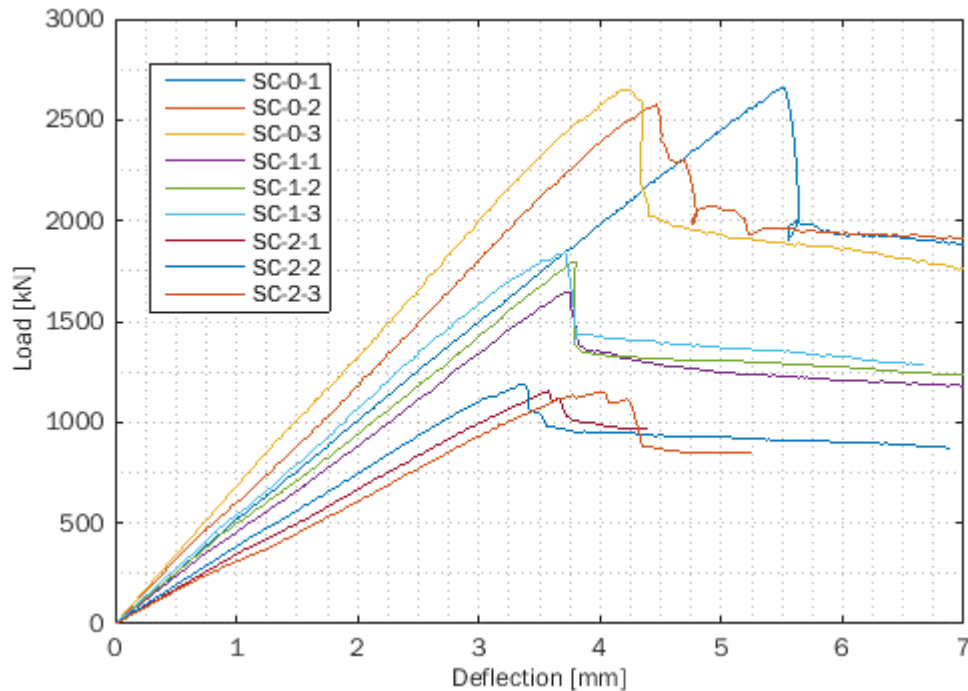


Figure 3.1-11 – Comparison of Load-Deflection-Curves.

Figure 3.1-11 shows a comparison of load-deflection curves. Excluding SC-0-1, the test results show comparatively small scattering of the repeated tests. Furthermore, with increasing eccentricity a smaller drop in the load bearing after maximum load can be observed.

Figure 3.1-12 shows a comparison of the strain evolutions in compression and tension cross-section axis. It can be seen that all the strain evolutions in the compression axis are running very similar independent of the chosen eccentricity level. The strain evolutions in the tension axis differ depending on the eccentricity. The greater the eccentricity is chosen, the lower is the compressive stress in the tensile axis. For a very large eccentricities tension strains can be observed in the tension axis.

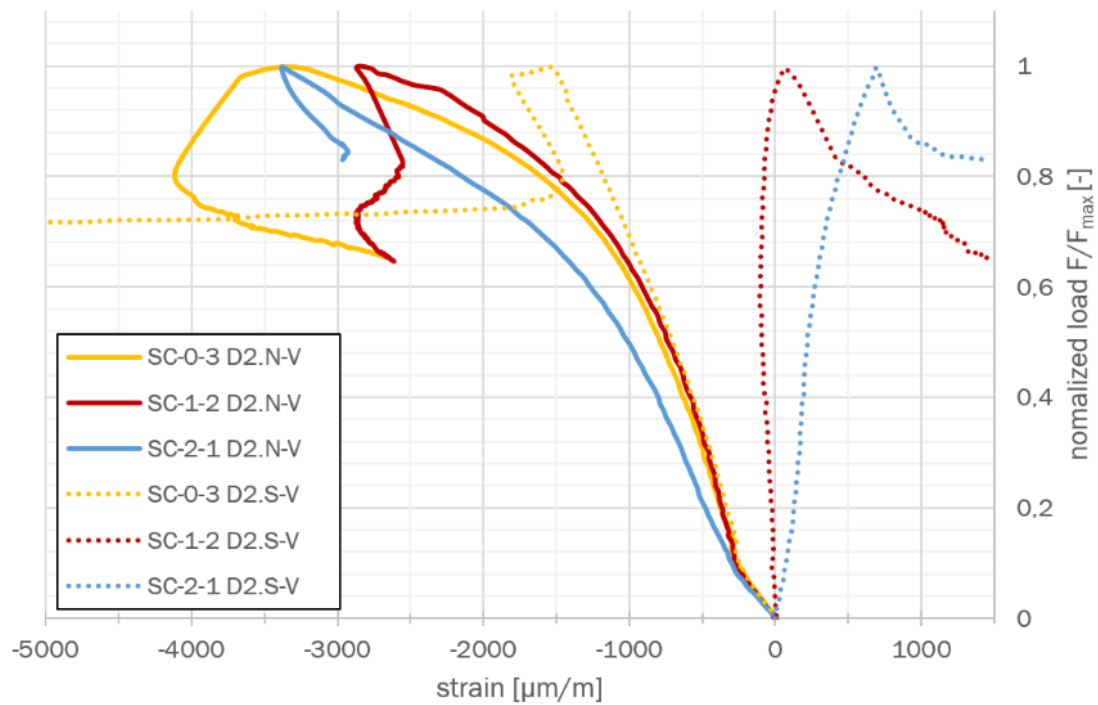


Figure 3.1-12 – Comparison between strain evolutions.

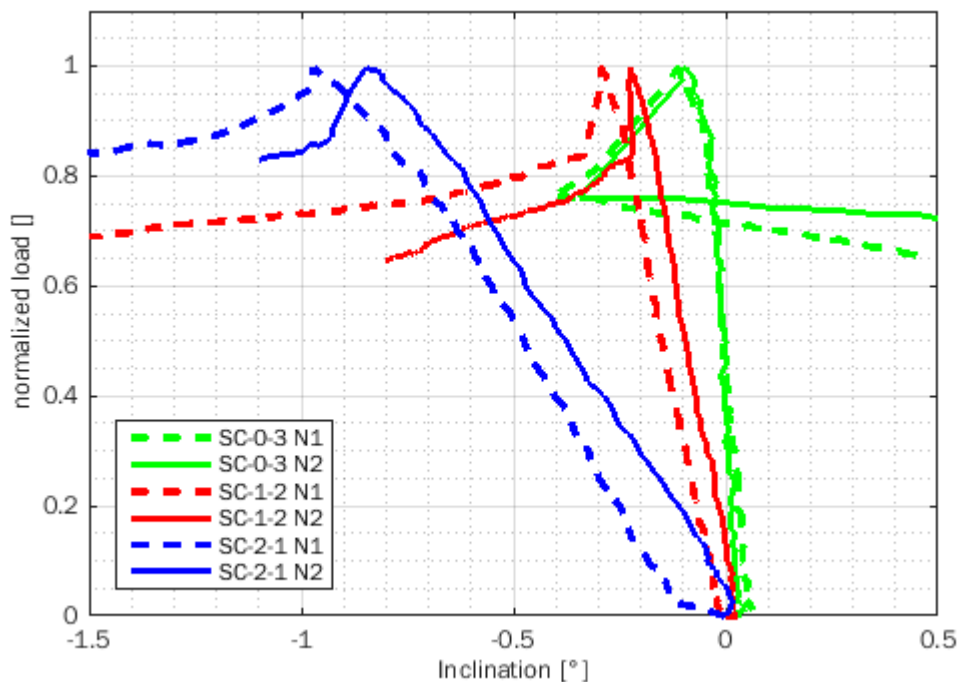


Figure 3.1-13 – Inclination evolutions.

Figure 3.1-13 shows the evolution of the measured inclination at the top and bottom of the representative specimen at different eccentricity levels. As requested, increasing eccentricity induces greater inclination. The very similar top and bottom inclination evolution suggests uniform and correct load input as well as small geometrical specimen imperfections from the production process.

### 3.1.4 Conclusion

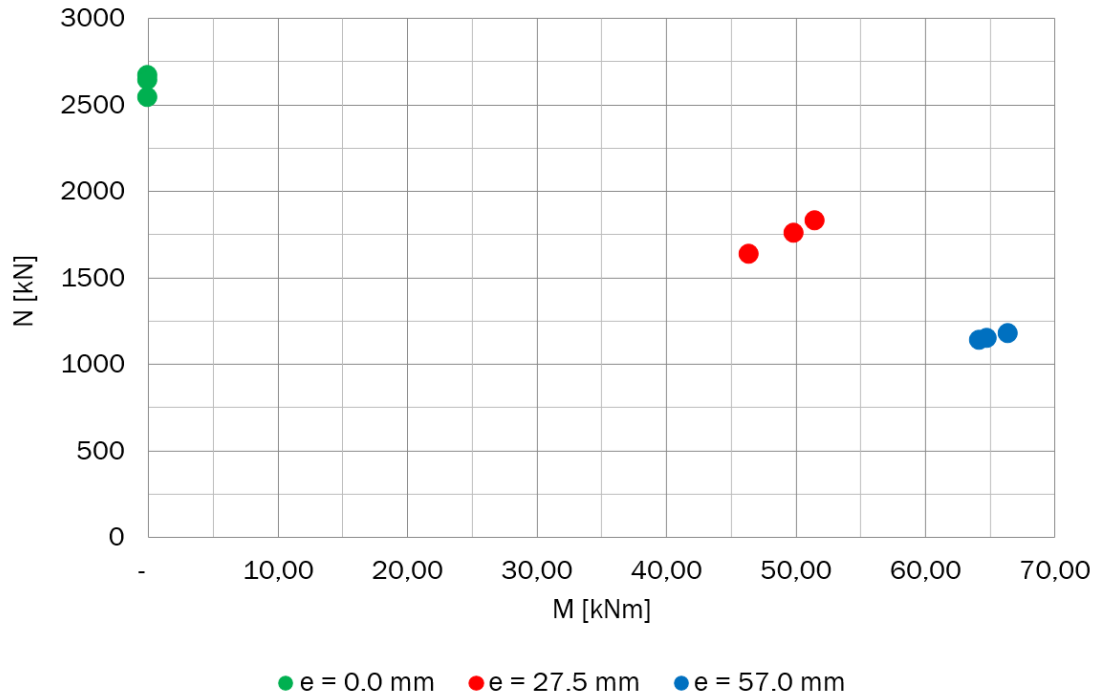


Figure 3.1-14 – Bending-compression interaction.

Figure 3.1-14 shows bending compression relationship of the tested specimens. The represented moment is calculated according to Equation Eq. 3.1-1.

$$M = e \cdot N \tag{Eq. 3.1-1}$$

Where:

- M Moment [kNm]
- N Axial load [kN]
- e Eccentricity [m]

The test results shown in Figure 3.1-14 correspond to the expectations considering engineering concepts. The presented production and testing process are very well suited to deal with the raised scientific issue. The obtained experimental data expand the knowledge of the structural behavior of sandwich tubes and pave the way for practical use as an innovation on component level. The represented experimental results will be incorporated into the Final Report D4.1.3 [3-03].

### 3.2 Sandwich material for connections and joints

While sandwich tubular construction can provide a structurally efficient solution by circumventing buckling limits, joining of sandwich steel structures provides a challenge. This can be for practical reasons, e.g. because of the two faces welding may be impossible for the inner face, simply because it is inaccessible. But also the fatigue strength that can be achieved may be an even more limiting factor than it is for conventional welded steel structures. The circumvention of buckling limits raises the allowable stress levels for the structures, which will result in fatigue becoming a more dominant design driver. Therefore high strength joining methods are needed. In [3-04] bonded joints were identified as a promising joining method for sandwich tubular steel structures. An important reason is that the two face layers of the sandwich provide a large area for stress transfer. Bonded joints can be made in many configurations, using one or two sides of the surface layers for bonding, and can even be combined with welding, see Figure 3.2-1.

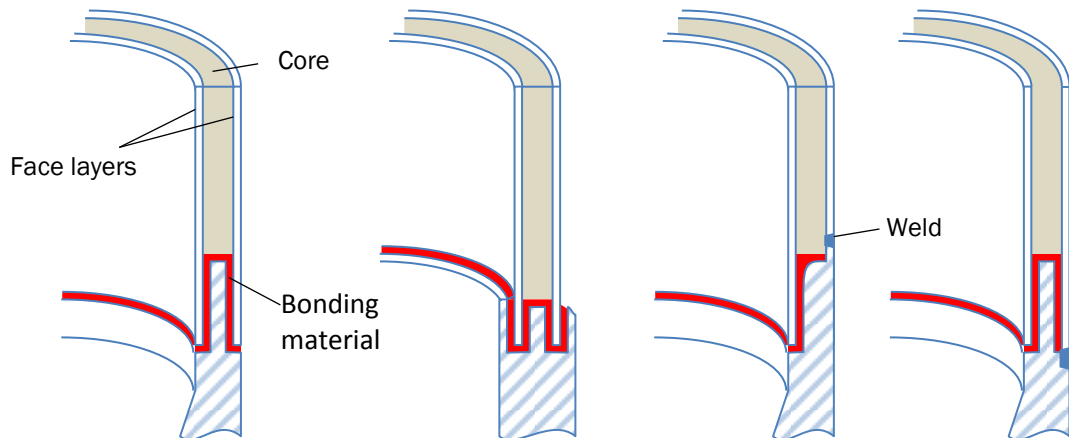


Figure 3.2-1 – Joint concepts for sandwich steel structures.

#### 3.2.1 Experimental programme on subcomponent – Joint test design

The aim of the subcomponent joint test design is to evaluate the behaviour of a full hybrid joint. For this purpose static and fatigue experiments are performed on hybrid joints subcomponents. First subcomponent hybrid joints coupons were designed, and in these experiments the load bearing capacity of bonded joints is evaluated, based on the stress levels in the steel tubes and previous steel joint tests. By comparing the stress levels in the steel tube the results can be related to joint strengths for e.g. welding (e.g.[3-05]).

For the experiments a symmetric metal-cement sandwich brace subcomponent coupon, with a double welded bonded connection to the grip system of WMC's 1MN testing machine was designed. Subcomponent coupons were manufactured in-house, and a manufacturing procedure was developed based on the procedure presented [3-06]. Static and fatigue tests were performed in order to evaluate the mechanical performance of the hybrid joints and compare the results to the previous bonded steel joint tests [3-04]. According to DNV/GL guidelines bonded joints must be designed for shear allowables of 1MPa in fatigue, and subcomponent static and fatigue tests need to be performed.

The tests were performed on subcomponent coupons 500 mm long, built with two concentric steel pipes with concrete in the middle as metal-cement sandwich structure. At the top and bottom of the sandwich, a metal transition part (interface with the test machine) is bonded with a double walled connection. The transition part included 8 threaded holes which were used to connect the

coupon to the testing machine. Exact nominal dimensions of the coupon and the transition part can be seen in Figure 3.2-2 and Figure 3.2-3 respectively.

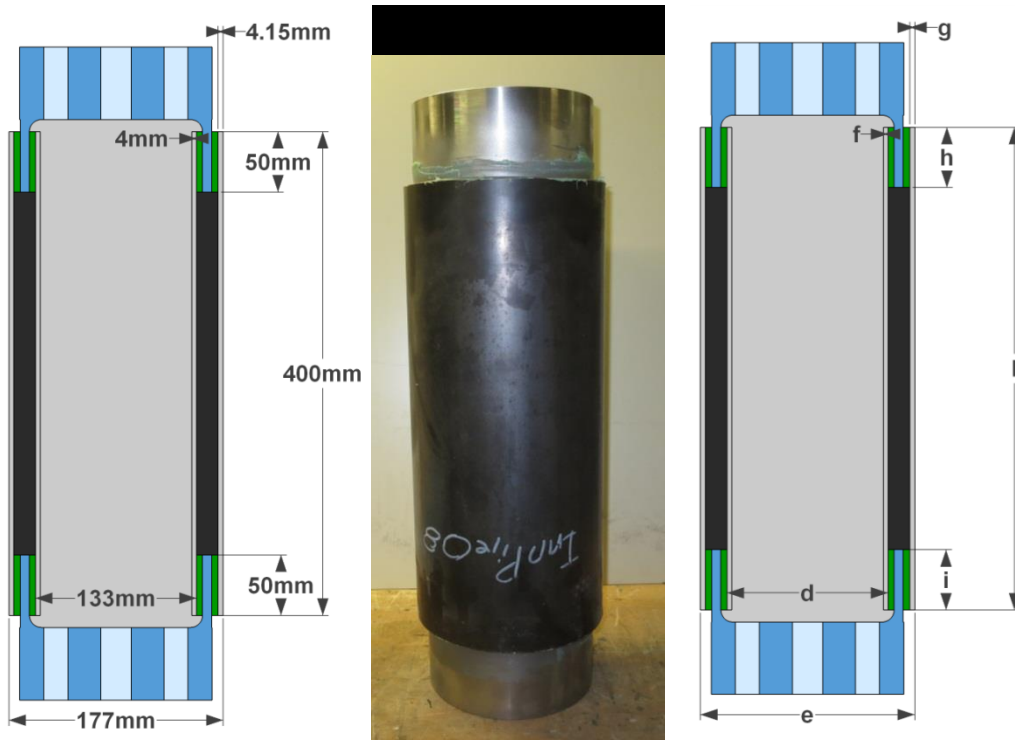


Figure 3.2-2 – Subcomponent joint tests coupon (left: nominal dimensions; right: dimension codes, see Table 3.2-1)

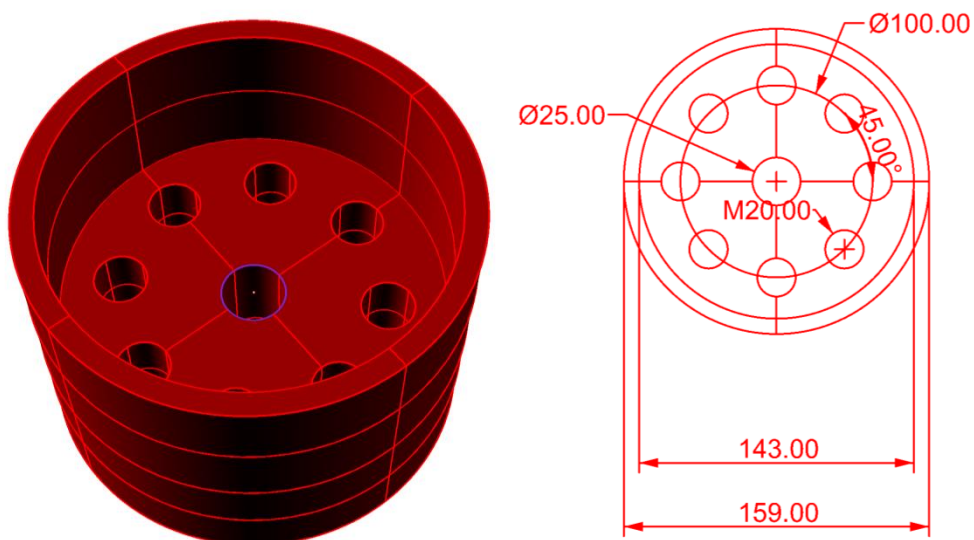


Figure 3.2-3 – Subcomponent joint tests coupon transition part.

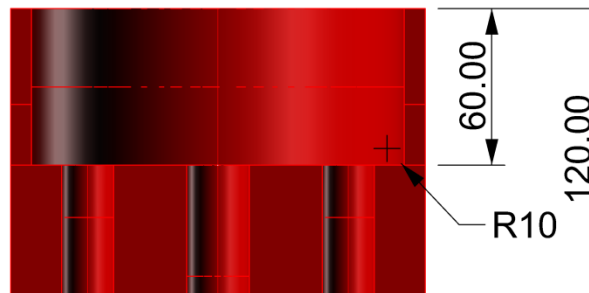


Figure 3.2-4 – Subcomponent joint tests coupon transition part.

The manufacturing of the coupons was carried out in two main steps; the manufacturing of the metal-cement sandwich structure and the bonding of the transition parts. The steps followed in the manufacturing process of the coupons are the following:

1. With a CNC machine two concentric rings with the steel pipes dimension were milled into a PVC ( $60 \text{ kg/m}^3$ ) foam panel with dimensions  $250 \times 250 \text{ mm}$ . Such milled rings allowed to position both steel pipes concentrically with a close tolerance. The rings were milled with a depth of  $50 \text{ mm}$  (Figure 3.2-4).

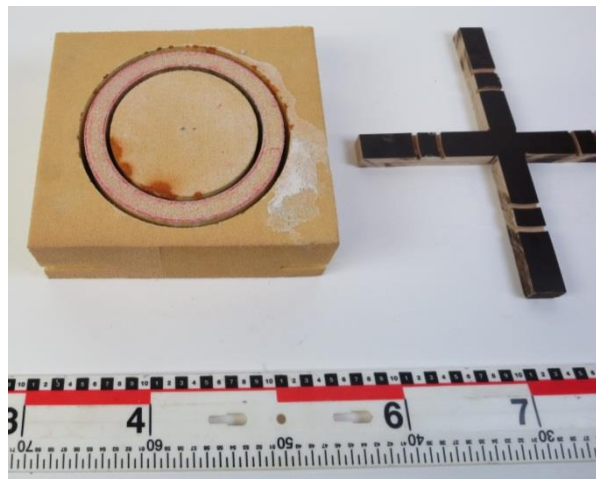


Figure 3.2-5 – Foam insert milled with a milling machine.

2. Position of steel pipes in the foam insert with a concentric close tolerance (Figure 3.2-5).



Figure 3.2-6 – Position of steel pipes in the foam insert.

3. The space between the steel pipes was filled with the concrete recipe [3-04] until the defined level (see Figure 3.2-2). With this system, at both sides of the steel pipes a gap of 50mm deep was obtained (Figure 3.2-6 and Figure 3.2-7).



Figure 3.2-7 – Metal concrete sandwich pipe.

- The steel fixture part was sandblasted to treat the surface and improve the adhesion with a 300micron sand powder (Figure 3.2-8).



Figure 3.2-8 – Transition part sandblasted (left). Sand blasting machine (right).

- The gap between both steel pipes was filled with Momentive EPIKOTE™ Resin MGS® BPR 135G-Series with EPIKURE™ Curing Agent MGS® BPH 134G-137G, and the sand blasted transition parts were bonded to the metal-concrete sandwich structure simultaneously. The top transition part was supported during bonding with the two columns shown in Figure 3.2-9. Parallelism tolerances smaller than 0.2 degrees were measured. 50 mm overlap length was used with a 45° degree fillet of adhesive on the outside and on both sides.



Figure 3.2-9 – Coupon bonded on both sides.

Table 3.2-1 – Measured dimensions.

	l	h	i	g	f	d	e
	(mm)	(mm)	(mm)	(mm)	(mm)	(mm)	(mm)
InnPipe01	400.0	49.6	58.4	4.1	4.0	133.1	177.0
InnPipe02	400.0	50.0	57.8	4.1	4.0	133.1	177.0
InnPipe03	400.0	56.9	48.7	4.1	4.0	133.1	177.0
InnPipe04	400.0	52.1	56.3	4.2	4.0	133.1	177.0
InnPipe05	400.0	49.3	54.1	4.2	4.0	133.1	177.0
InnPipe06	400.0	50.7	53.9	4.2	4.0	133.1	177.0
InnPipe07	400.0	51.9	27.3	4.2	4.0	133.1	177.0
InnPipe08	400.0	49.6	53.0	4.2	4.0	133.1	177.0
InnPipe09	400.0	51.6	54.3	4.2	4.0	133.1	177.0
InnPipe10	400.0	53.1	56.3	4.2	4.0	133.1	177.0
InnPipe11	400.0	57.7	53.3	4.2	4.0	133.1	177.0



Figure 3.2-10 – Test joint subcomponent coupons test setup.

Eleven joint tests coupons were manufactured and the main geometrical parameters were measured (see Table 3.2-1). For testing, a 1MN machine was used in pure axial testing loading. Three static tests were carried out at 1 mm/min until total debonding of one of the transition parts. The debonding area was calculated as the inner surface area plus the outer surface area (see Figure 3.2-11). In addition, fatigue tests at 2 Hz and loading ratio  $R=-1$  were carried out for the rest of the coupons.

### 3.2.2 Experimental test results

The static test results for all joint geometries and joint test subcomponent are listed in Table 3.2-2. Next to the force are the shear stresses in the adhesive. Figure 3.1-11 shows the stress-displacements curves for the three joint test subcomponent coupons, while coupon number 8 was discarded due to problems with the alignment during the testing. Stress-displacement curves show no drops of force until final failure which occurred as a sudden collapse, with no remarkable damage before final failure. In all cases the failure occurs at the bonding line of the inner pipe with a complete delamination and a fracture of the bonding line of the outer pipe (see Figure 3.2-12 and Figure 3.2-13). It is suspected that this behaviour occurred because the inner pipe has a smaller bonding area in comparison with the outer pipe.

Table 3.2-2 – Static test results.

	Load (kN)	Adhesive Shear stress (MPa)
50mm overlap with recess (compression)	269	20.4 (COV 8%)
50 mm overlap (compression)	219	16.9 (COV 12%)
100 mm overlap (compression)	344	13.6 (COV 14%)
50 mm overlap with fillet (compression)	354	27.7 (COV 2%)
Joint test subcomponent 50mm overlap (tension) (Un-cured, expired)	210	<b>5.4 (COV 18%)</b>
Joint test subcomponent 50mm overlap (tension) (Poor surface treatment & cured)	46	<b>1.2 (COV 48%)</b>
Joint test subcomponent 50mm overlap (tension) (Non-expired & cured)	198	<b>4.6 (COV 14%)</b>

When joint test subcomponents are compared with previous joint geometries tested, a strong reduction in strength is seen when compared with the 50 mm overlap with fillet but not if compared with 100 mm overlap coupons. Previous coupons were tested in compression, while these coupons have been tested in tension, which indicates that the configuration shows different allowables in tension than in compression. Other causes for this difference were studied, such as the surface condition and the curing of the adhesive. Table 3.2-2 shows that when the surface is not correctly treated, strong reductions in the ultimate strength might occur, however the curing of the adhesive or the expiration date did not show a strong influence. Other causes might lead to a decrease in the ultimate strengths such as a scaling effect or geometry effects.

These strong differences observed in the ultimate strengths in tension in comparison with the compression properties for the tested geometry, invite consideration of different adhesives than the tested one. Since the ultimate strength allowables condition the design of the joint, large bonding areas will be required.

An adhesive benchmarking tests campaign is recommended for further research in order to find the adhesive that performs better in this configuration. For that purpose a simplified double lap cylindrical coupon will be developed and used with different types of adhesives, where the same cylinder dimensions are considered in order to not underestimate the scaling effects.

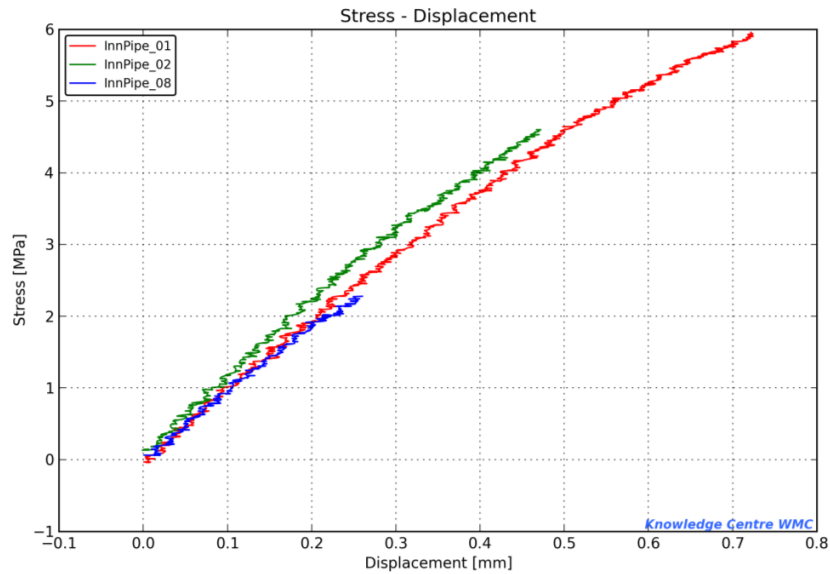


Figure 3.2-11 – Stress displacement curves. Joint-test subcomponent.



Figure 3.2-12 – Test joint subcomponent coupons InnPipe01 and InnPipe08 after static test.



Figure 3.2-13 – Test joint subcomponent coupons InnPipe01 failure details.

A limited number of fatigue tests were able to be performed on the view of the fatigue tests (Table 3.2-3). However, the three coupons that were tested showed a very poor fatigue life performance, in accordance with the results shown in the static tests and due to the same reasons described before.

Table 3.2-3 – Fatigue tests (R=-1).

	Fmax (kN)	Fmin (kN)	Smax (MPa)	Ncycles (cycles)	Tested Yes/No	Manufactured Yes/No
InnPipe09	146	-146	3.4	8	Yes	Yes
InnPipe10	146	-146	3.3	47	Yes	Yes
InnPipe11	56	-56	1.2	42945	Yes	Yes

### 3.2.3 Conclusions and recommendations

In the preliminary experiments described here the potential of bonding as a joining technique for tubular steel structures was evaluated. The results indicate that bonding could be a viable joining technique but a large effort in the development of the bonding process and to select the adequate bonding paste needs to be done. In these experiments single walled specimens were tested as well as sandwich tubes. Sandwich tubes showed lower ratios of surface layer thickness to overlap length and a large scatter was recorded in the overall tests. A significant difference appears between the shear stresses of the different types of coupons in compression and tension.

The large scatter observed was due to the bonding process and type of adhesive and geometrical configuration. Unless this is further tackled, large safety factors in the design of this type of joints can be expected. Further research in the selection of the adhesive is required in order to ensure processability and stability of the mechanical properties. In addition, further research is recommended in relation with the manufacturing process aiming to ensure the stability of the bonding line properties and the surface treatment via automation.

In order to improve the adhesive properties and design allowable an adhesive benchmarking tests campaign is recommended for further research, in which static and fatigue properties are evaluated. In a later stage, also the fracture energy density of the adhesive-steel interface will need to be further investigated.

## References

- [3-01] INNWIND.EU: Innovations on component level (interim report). Deliverable D4.1.2, 2015.
- [3-02] Lindschulte, Nick: Drucktragverhalten von Rohren aus Ultrahochfestem Beton mit Stahlblechummantelung, Dissertation, Berichte aus dem Institut für Baustoffe, Heft 10, Hannover, 2013 (in German).
- [3-03] INNWIND.EU: Innovations on component level (final report). Deliverable D4.1.3, 2015.
- [3-04] INNWIND.EU: Innovations on component level for bottom based structures. Deliverable D4.1.1, 2013.
- [3-05] BS 7608-1993 – „Code of practice for Fatigue design assessment of steel structures“, 1993.
- [3-06] Keindorf, C., “Tragverhalten und Ermüdungsfestigkeit von Sandwichtürmen für Windenergieanlagen”, Dissertation, Institute for Steel Construction, Leibniz University Hannover, 2010, (in German).

## 4 SOIL & FOUNDATION

Authors: Bo Ibsen, Lars (Aalborg Universitet - AAU)  
Kohlmeier, Martin; Foglia, Aligi (Fraunhofer-Gesellschaft Hannover – FhG-H)

### 4.1 Suction bucket foundations

Jacket structures are usually founded on piles, these foundations are of simple design but Bucket foundations are an option that can decrease the overall cost and increase the diffusion of wind turbine. Since wind turbine are dynamically sensitive structures where stiffness requirements have to be satisfied, an alternative design allowing to increase stiffness is multi-bucket configuration [4-01], wherein loading response changes significantly with respect to a mono bucket. The following work is focused on loading of multi-bucket foundation also referred to as multi-pod, where very little moment is taken by the bucket itself. The moment load is mainly resisted by push-pull load on the vertical axis of opposite buckets. For these reasons, it is important to understand behaviour under tensile loading and improve the stiffness of foundation, so more correct design methods can be established. Among others, multi-pod foundations can be either tripod or tetrapod. Tripod has the advantage that it requires less material and it is easier to construct and install. In [4-02] the focus has been to the static bearing capacity both in compression and tension of vertical loading of suction caisson installed in sand. Monotonic pull-out tests were conducted and specifying equipment used and test modality adopted in order to discuss and compare works of different researchers.



Figure 4.1-1 – Jacket structure with bucket.

During the life-time period of an offshore structure, repetitive loading is present. The cyclic burdening of these structures is generated by the environmental loads, such as the wind and wave actions. In this sub-section, experimental results of vertical axial loading cyclic tests of bucket foundation are presented, with performed ranges of up to 40.000 cycles with different load amplitudes and frequencies. The scope of the research is to analyse and observe the response of the foundation as an integer, by means of stiffness evolution and the accumulated vertical displacement - factors that are considered critical in the design of a skirted foundation.

Having this purpose, a ~ 1:10 scaled footing model with an embedment ratio  $d/D$  of 0.5 is used during the entire research at Aalborg University Geotechnical Laboratory. The applied vertical cyclic loads are either only tensile or two way tensile-compressive. The accumulated upward displacement was found to be dependent and strongly affected by the characteristics of the cyclic loading. Results are presented to give a clear idea on how the change in stiffness and accumulated displacement due to the long-term cyclic loading affects the footing.

### 4.1.1 Experimental Details

In this sub-section, experimental tests and results of medium-scale bucket foundation tested in dense sand is presented. Each test has four stages: 1) soil preparation, 2) footing installation, 3) initiating cycle loadings and 4) post-cyclic pull-out. A detailed description of the preparation of the sand to obtained high compaction level, are presented in [4-03].

The soil classification parameters for the Aalborg University Sand No. 1 are described in Table 4.1-1. Aalborg University Sand No. 1 is quartz sand with fines content of less than 1%.

**Table 4.1-1 – Characteristic properties of Aalborg University Sand no.1**

Characteristic	Symbol	Value
50% quantile [mm]	$d_{50}$	0.14
Coefficient of uniformity [-]	$d_{60}/d_{10}$	1.78
Specific grain density [ $g/cm^3$ ]	$d_s$	2.64
Maximum void ratio [-]	$e_{max}$	0.858
Minimum void ratio [-]	$e_{min}$	0.549

Once the soil preparations are completed, the density is checked by using a small laboratory cone penetration test. Before the installation of the bucket in the prepared sandbox, four CPTs were performed with velocity of 5 mm/s. Typical cone data is shown in Figure 4.1-4. The cone diameter is 15 mm, with cross-sectional area of 176.7 mm<sup>2</sup> and an inclination angle of the cone of 60°. The most important parameters obtained from the measured CPT data are relative density  $D_r$ , and the friction angle  $\phi$ , as shown in Table 4.1-3. Further, it was possible to determine the effective unit weight.

Figure 4.1-2 shows the testing rig and further mechanical details can be found in [4-03]. The loading control system used in all the tests has two options for applying the load: by displacement or by force. The static loading tests, was displacement controlled, whereas the cyclic loading tests was force controlled. The system needs to apply displacement in order to provide the desired force, which is controlled by a transducer that transmits feedback to the program output.

The response of the footing was measured by the load cell U10M from HBM for the resulting forces and by two ASM GmbH position transducers located on a beam above the footing (as seen in Figure 4.1-3), measuring the precise displacement to secondary CPU. Membrane pressure was measured by a separate transducer also connected to the HBM Spider with the rest of the transducers. All the recorded data, such as force and displacement were sampled with 2 Hz rate during testing. The sign convention chosen to work with the displacement and the forces is presented in Figure 4.1-5. The loading point is centrally positioned.



Figure 4.1-2 – Loading rig with installed bucket foundation and applied overburden pressure on the soil surface.

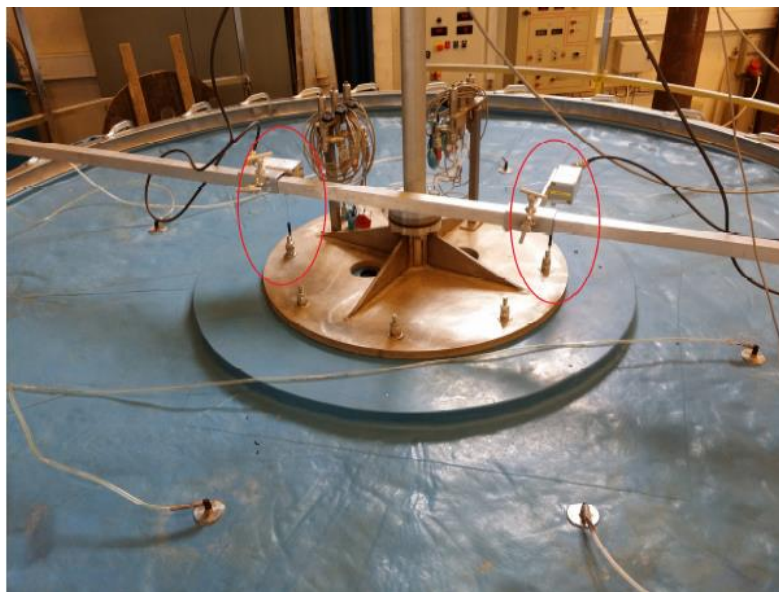


Figure 4.1-3 – Position of the two displacement transducers during loading

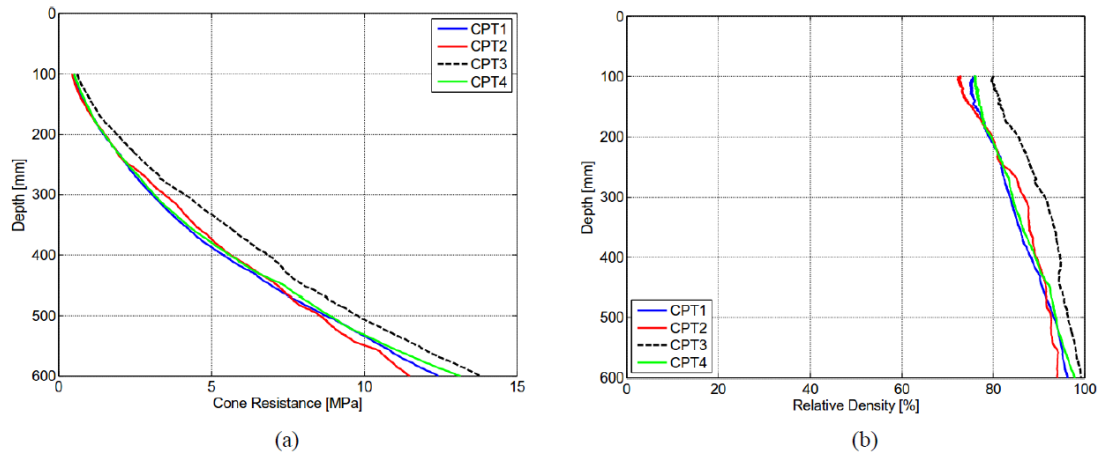


Figure 4.1-4 – Cone interpretation for Test No. 130315, before pressure application: a) CPT Cone resistance  $q_c$ ; b) Relative Density  $D_r$  ( $\sigma_1 = 6.59$ ;  $\sigma_2 = 6.62$ ;  $\sigma_3 = 5.76$ ,  $\sigma_3 = 6.70$ ).

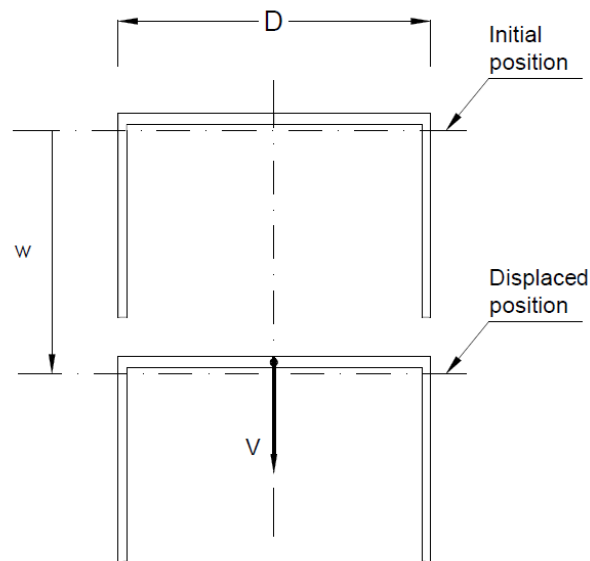


Figure 4.1-5 – Sign convention for displacement and force.

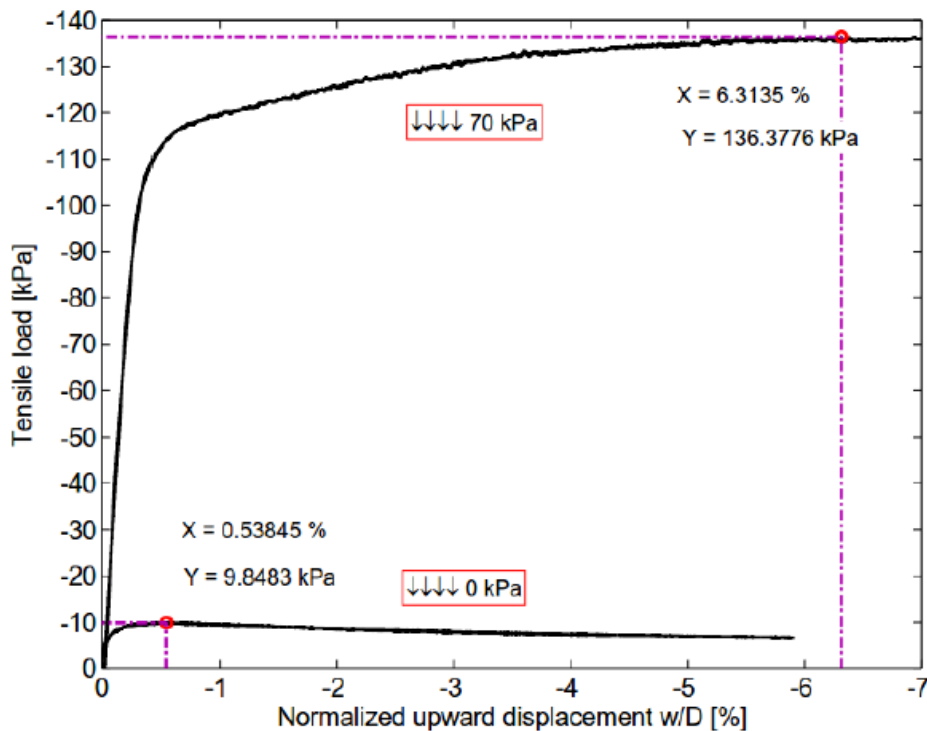


Figure 4.1-6 – Reference monotonic pull-out tests with 0 and 70kPa pressure on the soil surface.

#### 4.1.2 Experimental test program

Before describing some of the testing phases, it is important to mention that some of the key elements of the framework used to analyse the data is similar to the empirical model described in [4-04] and [4-05]. Relationships between number of cycles  $N$ , and normalized accumulated displacement  $w/D$ , are chosen as the main parameters describing the foundation behaviour. The work conducted in this test program consists of vertical monotonic and vertical cycling loading tests. Initially, the reference monotonic pull-out loadings were carried out in order to determine the maximum force (capacity) acting on the foundation as it can be seen in Figure 4.1-6.

At the end of each cyclic test, post cyclic phase was performed in order to measure the post-cyclic behaviour. From the limited pull-out displacement due to the position of the displacement transducers, not all tests have post-cyclic phases. Example for two reference monotonic pull-out tests with a bucket of  $d/D = 0.5$  is shown in Figure 4.1-6. The tests are performed with 0 kPa and 70 kPa overburden pressure. A clear difference can be seen in terms of the ultimate tensile loads and of displacements. The peak tensile load with overburden pressure equal to 0 kPa was mobilized at the displacements of 0.5% bucket diameter, whereas the peak tensile load with pressure of 70 kPa at 6.3% bucket diameter.

As a comparison, some additional data for tests with overburden pressure of 20 and 40 kPa show small displacement mobilizations at 0.4-0.9% bucket diameter [4-03]. Reasonable explanation for the reference monotonic test with 70 kPa pressure might be that the force acting from the membrane itself gives contribution to the mobilization capacity.

**Table 4.1-2 – Test program overview**

Test name	External Overburden pressure [kPa]	Performed CPT's	f [Hz]	$V_{\text{mean}} \pm V_{\text{amp}}$ [kPa]	$\zeta_b$	$\zeta_c$	No. of cycles	Post-cyclic pull-out
Static reference monotonic pull-out tests								
130215	0	4	static	-	-	-	-	-
130217	70	4	static	-	-	-	-	-
Cyclic axially loaded tests								
130310	0	4	0.1	-5.1±2.51	0.78	0.35	39 753	N/A
130312	0	4	0.1	-5.1±4.88	1.0	0.02	1 284	N/A
130313	70	4	0.05	-0.45±37.43	0.28	-0.97	19 716	N/A
130314	70	4	0.1	0.13±36.4	0.25	-1.0	39 703	Yes
130315	70	4	0.1	-34.5±29.3	0.47	0.08	24 637	Yes
130316	70	4	0.1	-71.9±31.2	0.75	0.40	18 984	N/A
130317	70	4	0.1	-70.4±58.1	0.94	0.10	5	N/A
130319	0	4	0.1	-2.67±2.1	0.49	0.12	32 633	N/A

Based on these reference pull-out tests, all cyclic amplitude were calculated for the upcoming cyclic tests. All tests presented in this study can be seen in Table 4.1-2 where the full list of the test names and detail specifications are given. Related data for the interpretation of the conditions of the soil before installation of the Bucket are presented in Table 4.1-3.

It can be seen, that all the tests were performed in the range of dense to very dense sand. The friction angle indicates high value, as main cause for this, are the low mean stresses acting in such shallow depths, fact which can be observed in the Mohr- Coulomb failure envelope.

Common usage of non-dimensional groups are observed in similar test programs, e.g. [4-06], but during this test program the only non-dimensional group used is the displacements occurring due to the loadings and normalized with the bucket diameter.

**Table 4.1-3 – Compaction level and preparation conditions estimated by CPTs average for depth of 600 mm.**

Test No.	CPT Relative Density $D_r$ [%]	CPT Friction Angle $\phi$ [°]	Effective soil unit
130215	85	53.6	9.60
130217	83.8	53.4	9.53
130310	N/A	N/A	N/A
130312	78.6	52.6	9.28
130313	82.9	53.2	9.49
130314	82.4	53.1	9.46
130315	87.5	53.95	9.71
130316	79.8	52.77	9.34
130317	81.5	53.0	9.42
130319	79.2	52.7	9.31

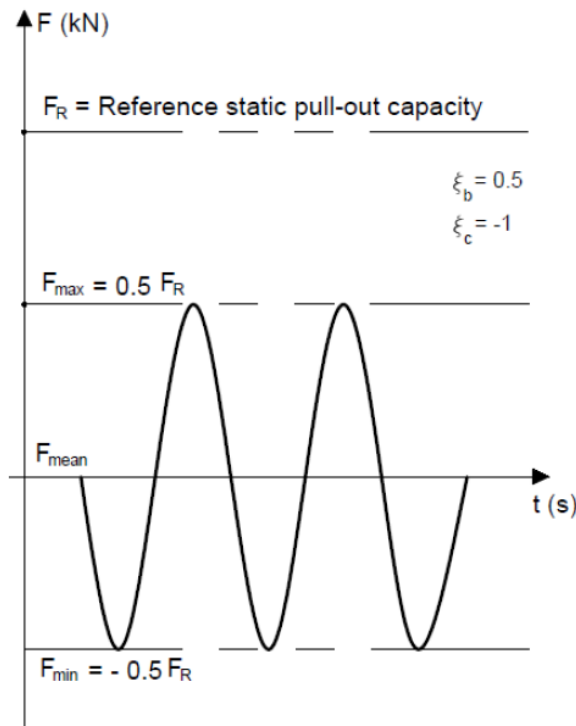


Figure 4.1-7 – Example of two-way tension/compression loading.

It is intentionally chosen to do so, as results can be used for future comparison. In order to reduce the cyclic test program, as time to perform one cyclic test take up to 8 days, consistent attention was accounted. To do so, different amplitudes and mean loadings were chosen with respect to the reference monotonic tests.

[4-04] and [4-05] defines two specific cyclic parameters  $\zeta_b$  and  $\zeta_c$  witch can characterize the applied cyclic loads, defined as shown in Eq. (1) and illustrated in Figure 4.1-7 and Figure 4.1-8.

$$\zeta_b = \frac{F_{max}}{F_R}, \quad \zeta_c = \frac{F_{min}}{F_{max}} \quad (1)$$

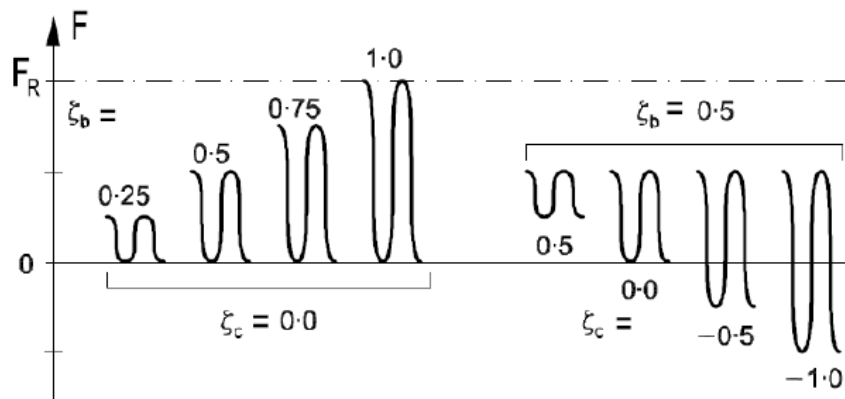


Figure 4.1-8 – Characteristics of cyclic loading defined in terms of  $\zeta_c$  and  $\zeta_b$ , after [4-05].

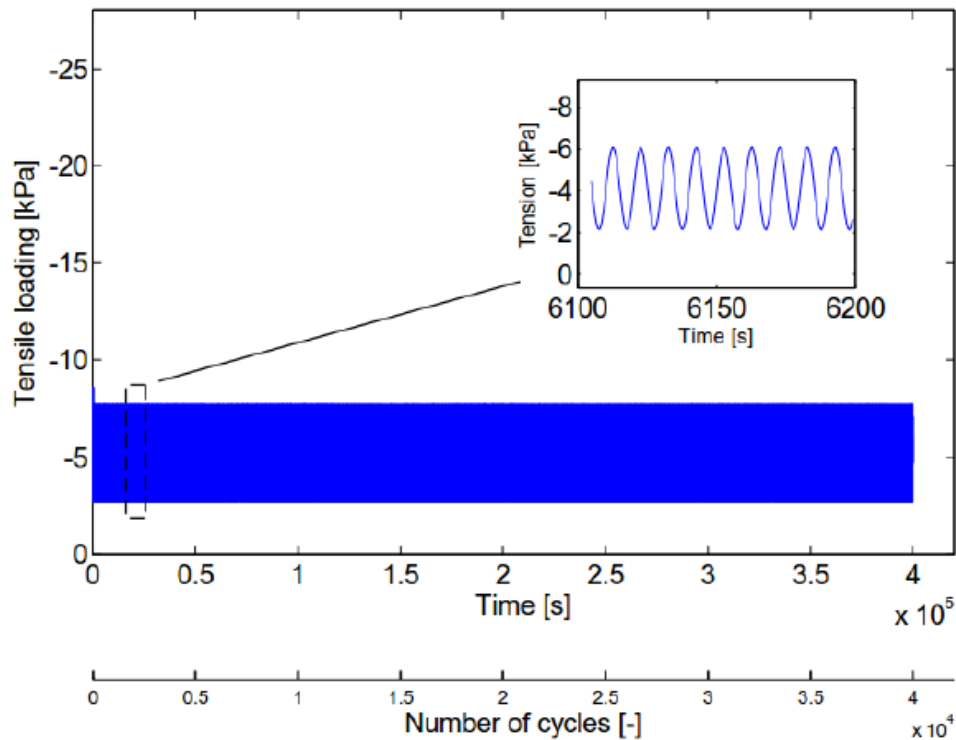


Figure 4.1-9 – Sinusoidal type of loading for Test. 130310 and magnifying view of few cycles.

where  $F_{max}$  and  $F_{min}$  represent the maximum and the minimum force in a loading cycle, as presented in Figure 4.1-7 and the  $F_R$  is the force at failure obtained from the reference monotonic pull-out test. According to [4-05], the dimensionless parameter  $\zeta_c$  gives information about the characteristics of the cyclic load and takes the value of 1 for a static test, 0 for one-way loading and -1 for two way loading (tension and compression). On other hand,  $\zeta_b$  gives information about the size of the cyclic loading normalized with respect to the reference monotonic capacity, as follows:  $0 < \zeta_b < 1$ . The load ratios are illustrated in Figure 4.1-8.

### 4.1.3 Results

This sub-section describes the behavioural of a bucket foundation with embedment ratio  $d/D = 0.5$  under vertical cyclic loading. Positive loads are compressive tensile loading and negative. Positive displacements define settlement and negative displacement express upward movement. Figure 4.1-9 simply shows how the loading occurs during one of the test with 0 kPa external overburden pressure in terms of time and number of cycles. Additionally to this, it can be seen that the test is performed only in tensile regime. The maximum amount of cycles that can be generated (40,000) which are limited by the loading control system MOOG. The duration of the cycles loading phase is approximately to 5 days.

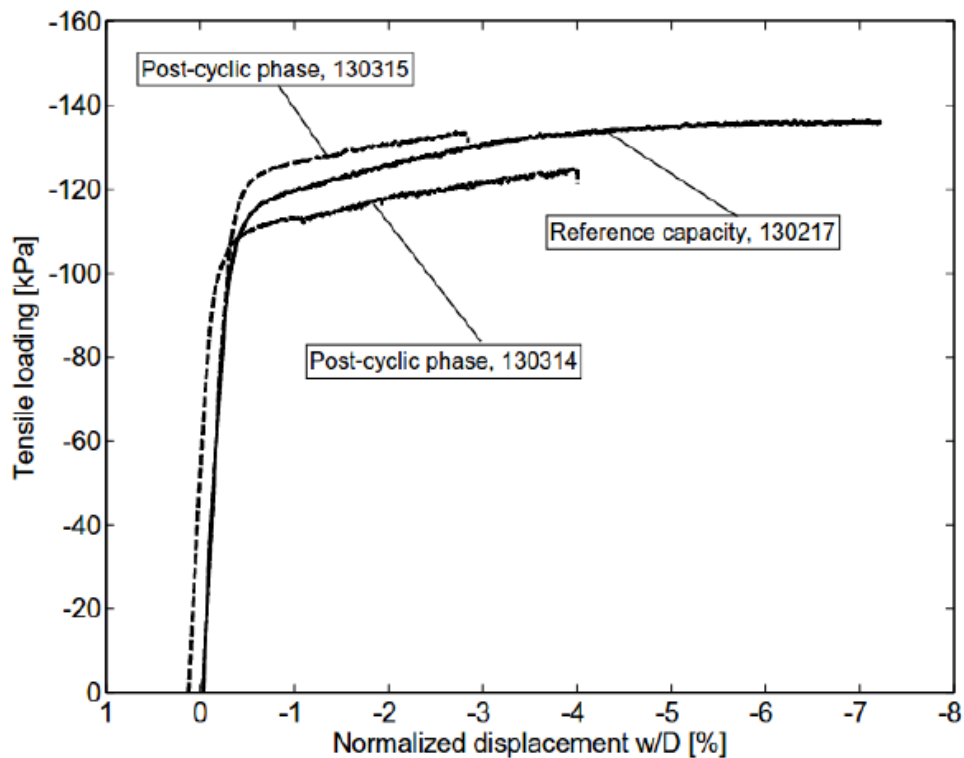


Figure 4.1-10 – Reference monotonic test 130317 and post-cyclic phase for 130315 and 130314 all perform with 70 kPa overburden pressure.

In Figure 4.1-10, the reference monotonic test 130217, with overburden pressure of 70 kPa is plotted. It clearly shows that general failure mechanism is developed, with a soft peak followed by stable branch of data points. On other hand tests 130314 and 130315, did not show a distinct peak in force capacity. It is observed that the post-cyclic phase for the two-way loaded test (130314), appear to show decrease in the loading capacity. For the post-cycle phase of the test (130315), with loading ratio of  $28.2 \pm 21.5\%$ , the pattern is very close to the reference path, but with small increase of the force capacity in the first part of the phase, which may be due to stiffening up of the soil.

#### 4.1.4 Tensile cyclic loadings with different overburden pressure.

Valuable information concerning how the accumulated displacement in terms of number of cycles is changing when applying different amplitudes is presented. Method used for determination of the accumulated displacement is approached in the same way as [4-04]. Four out of the six tests that are comparable for this purpose are chosen. These tests have a starting point of mean load corresponding to 50% of the reference monotonic test for 0 and 70kPa, respectively, but using different amplitudes corresponding to 25% and 50%. In Figure 4.1-13 to Figure 4.1-16, it is in detail shown how the accumulated upward displacement with respect to the acting load amplitude develops.

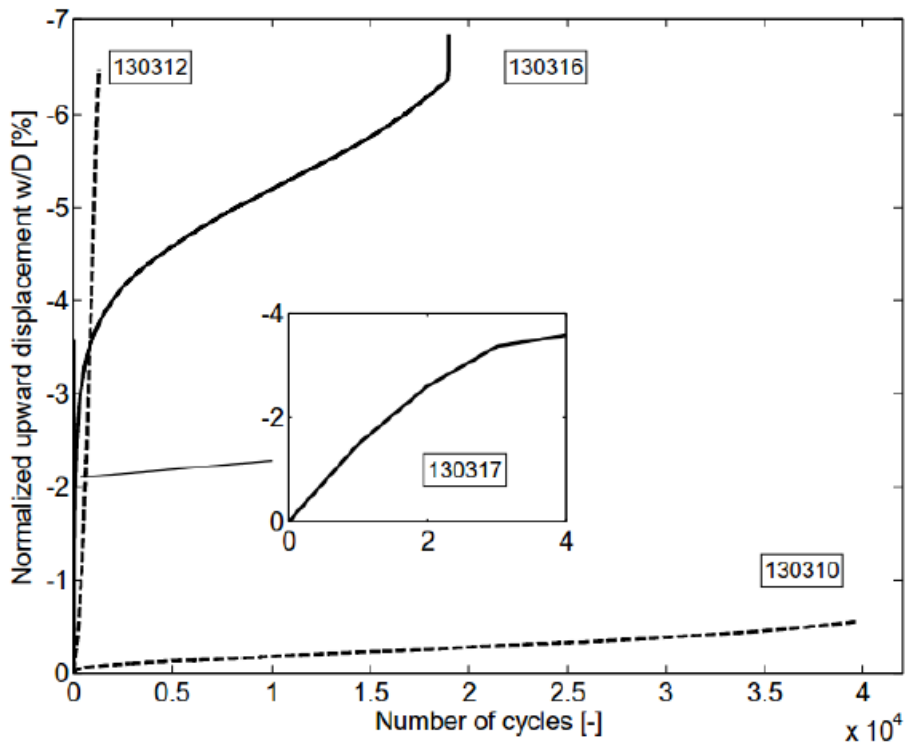


Figure 4.1-11 – Accumulated normalized upward displacement in respect to number of cycles (dashed – 0 kPa tests; solid – 70 kPa tests)

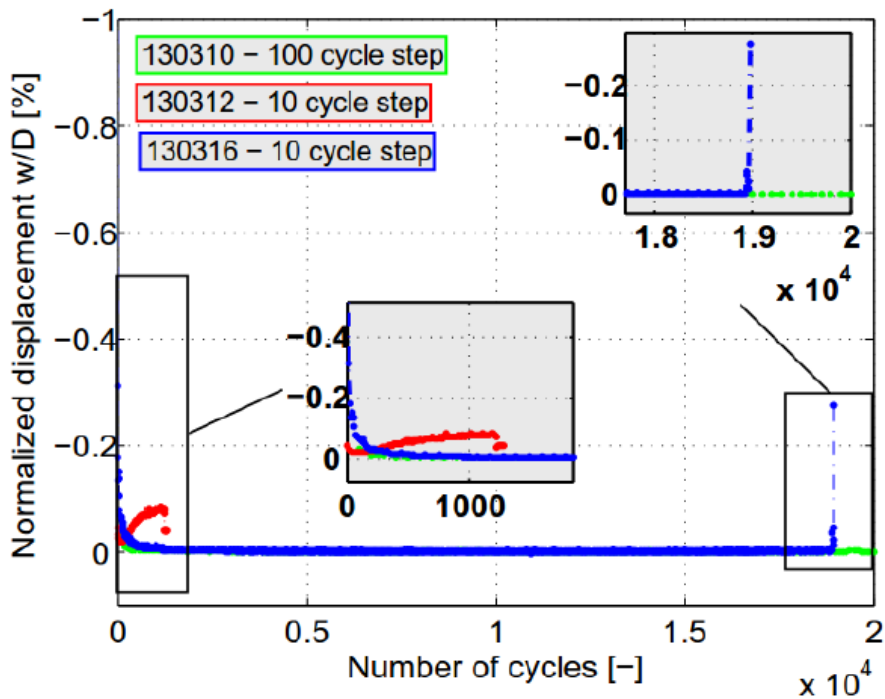


Figure 4.1-12 – Rate of accumulated normalized displacements in terms of number of cycles. Tests No.: 130310, 130312, 130316 and magnifying view of the initial phase.

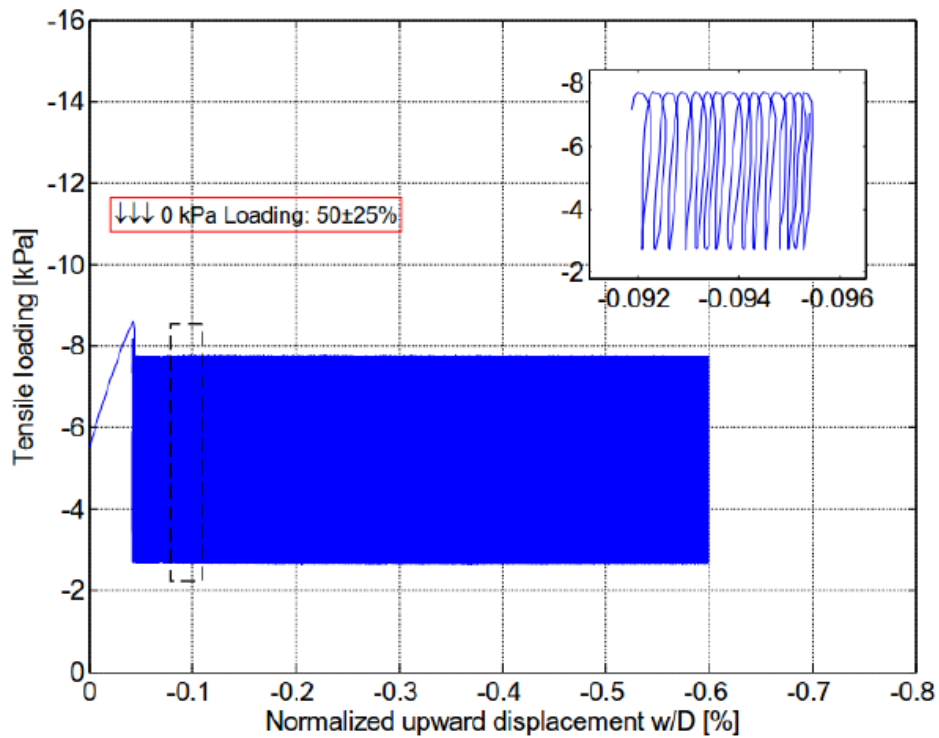


Figure 4.1-13 – Normalized upward displacement in respect to tensile loading. Test. 130310 and magnifying view of few cycles.

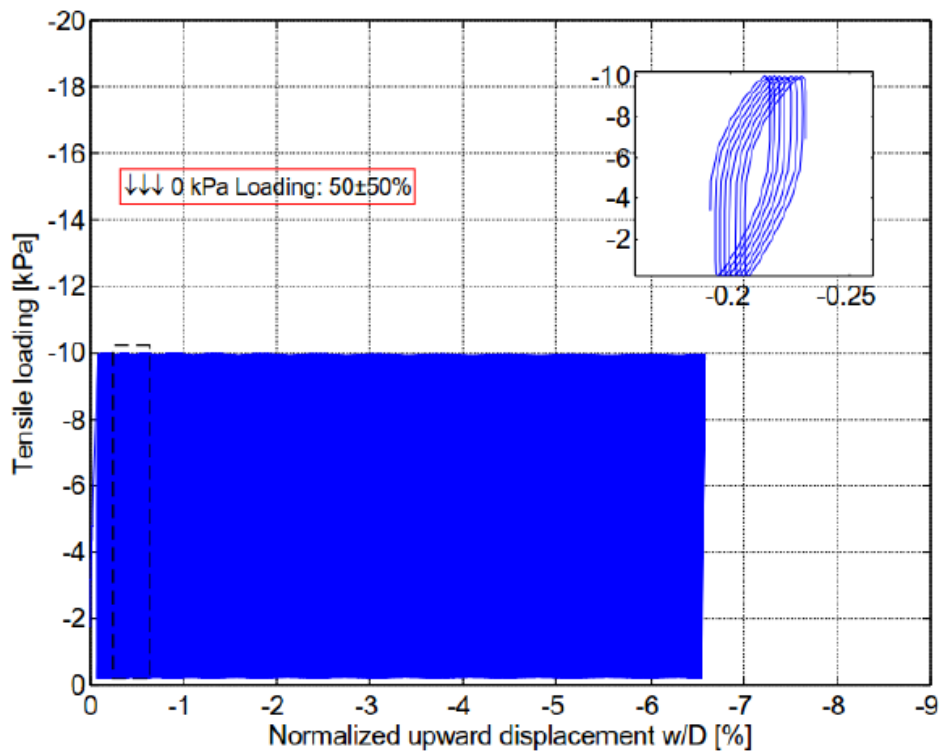


Figure 4.1-14 – Normalized upward displacement in respect to tensile loading. Test. 130312 and magnifying view of few cycles.

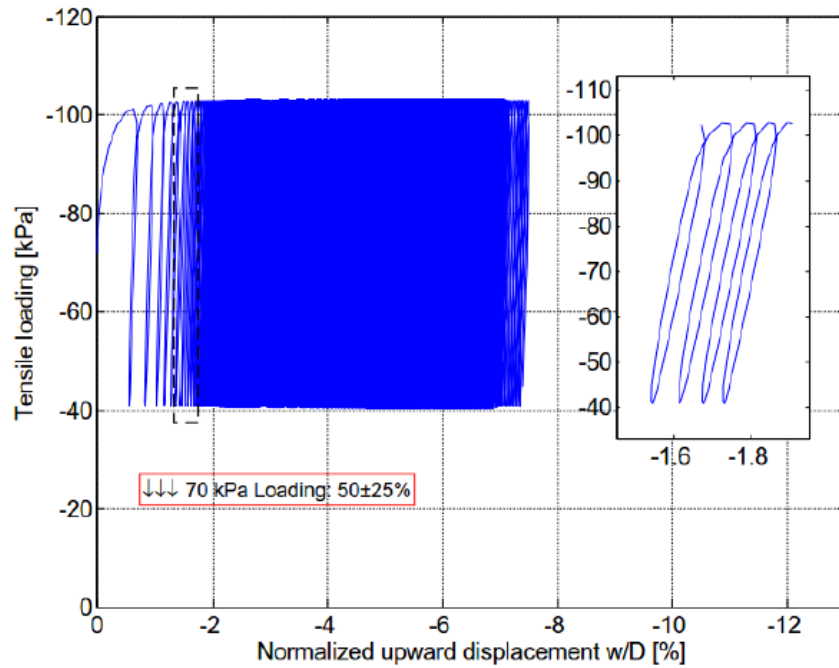


Figure 4.1-15 – Normalized upward displacement in respect to tensile loading. Test. 130316 and magnifying view of few cycles.

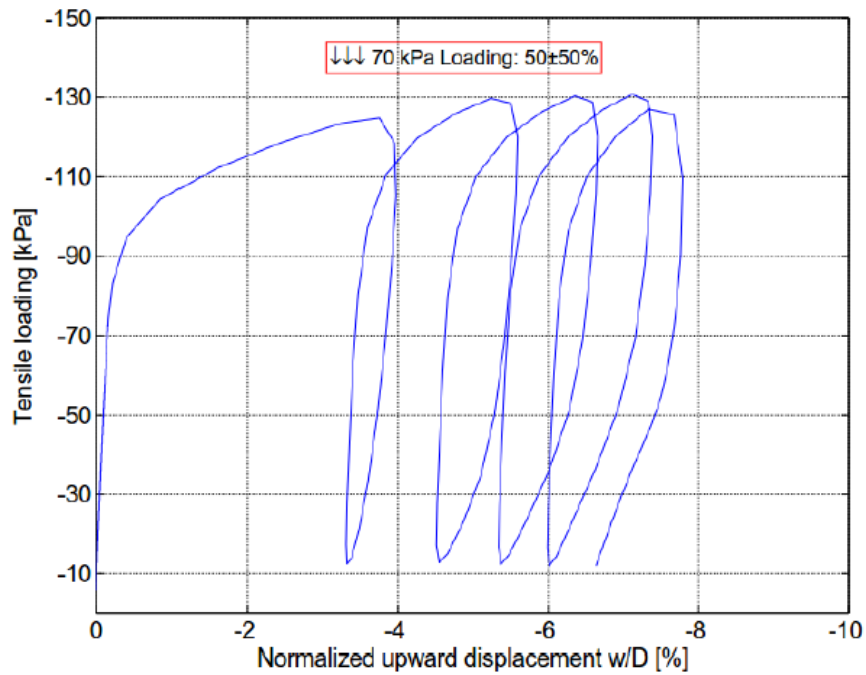


Figure 4.1-16 – Normalized upward displacement in respect to tensile loading. Test. 130317 with duration of less than 5 min. due to the high amplitude.

Figure 4.1-11 shows the load amplitude influence on tests with 0 and 70 kPa overburden pressures. The figure shows, how the number of cycles changes in this tests. When comparing the two tests with 0 kPa (dashed lines). It is seen, that the cyclic loading, with amplitude of 50%, reaches upward normalized displacement  $w/D$  equal to 0.5%, 159 times faster than the cyclic loading with amplitude of 25%. This response gives good understanding on how load amplitudes from waves can act on real offshore footing and how important this information is. When comparing the two tests with 70 kPa (solid lines). It is seen, that the cyclic loading, with amplitude of 50%, reaches upward normalized displacement  $w/D$  3.58%, 236 times faster than the cyclic loading amplitude of 25%.

Figure 4.1-12 shows the rate of the normalized upward displacement  $w/D$ , i.e. permanent displacement every hundred cycles,  $\delta a_{N+100} - \delta a_N$  and another test for every ten cycles,  $\delta a_{N+10} - \delta a_N$ . These values are plotted against  $N$  for three tests in tension regime. Test 130312 has less than 1300 cycles, therefore, the step was chosen to  $N+10$ . In general, when the rate of accumulated displacement increases with the number of cycles, it indicates a progressive failure. For the tests shown in Figure 4.1-12, this is not occurring. It can be seen that significant accumulated displacement  $\delta a$ , occurs within the first 2000 cycles and followed by stable plastic adaption ending up reaching negligible values.

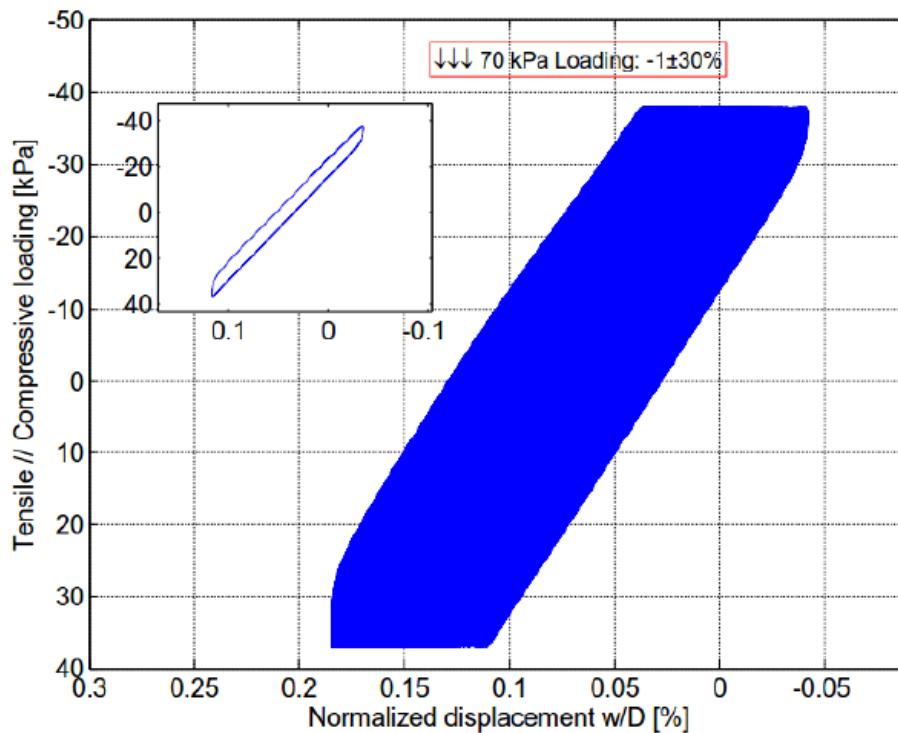


Figure 4.1-17 – Normalized upward displacement in respect to two-way loading. Test. 130313 and magnifying view of few cycles.

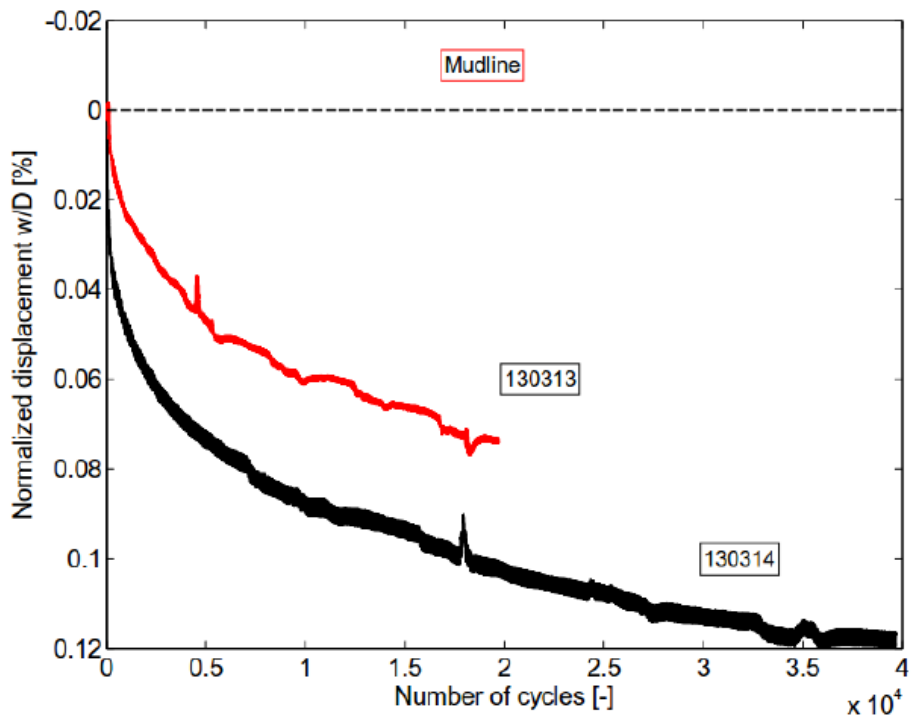


Figure 4.1-18 – Comparison between test with loading frequency of 0.05 Hz (Test No. 130313) and 0.1 Hz (Test No. 130314). Visible settlement due to the compressive loading.

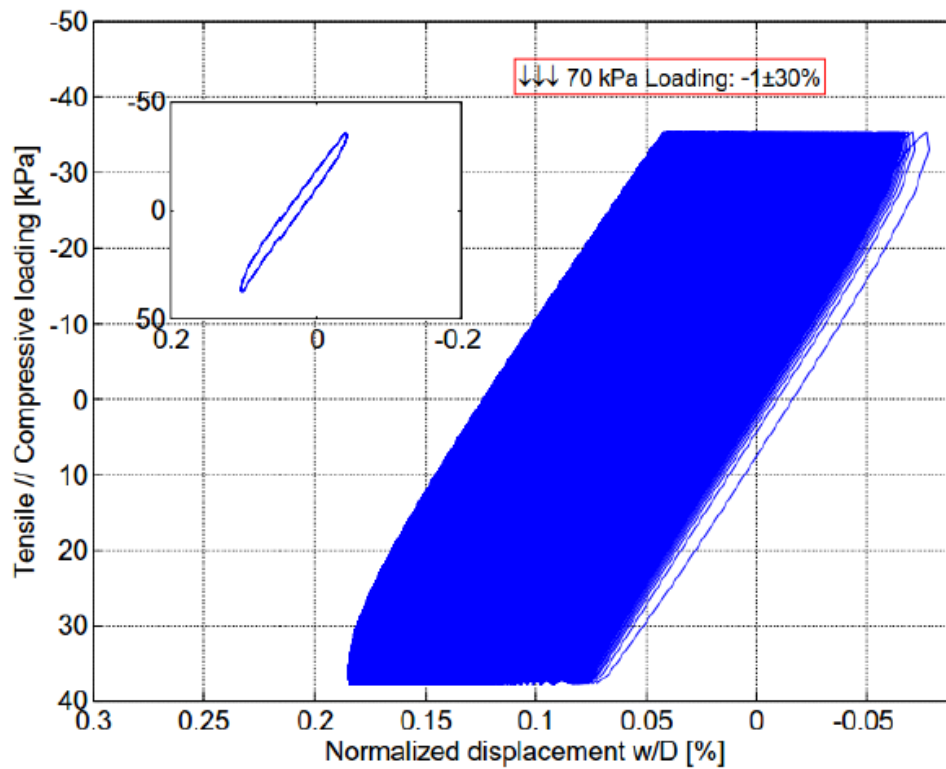


Figure 4.1-19 – Normalized upward displacement in respect to two-way loading. Test. 130314 and magnifying view of few cycles.

#### 4.1.5 Loading rate effect from two-way loading in tension and compression

The influence of loading rate on the development of permanent deformations has also been investigated by performing two tests in two-way loading phase (tension and compression). The test was performed with load frequency of 0.05 and 0.1 Hz. The vertical load, for both tests were corresponding to  $V_{min} = -1$  kPa and  $V_{amp} = \pm 30\%$  of  $V_{failur}$  close to 1% amplitude difference. Both test with less than 1% different in terms of  $D_r$ ,  $\phi$  and  $\gamma'$ , dense sand ( $D_r = 82.6\%$ ,  $\gamma' = 9.47$  kN/m<sup>3</sup>). The applied overburden pressure was 70 kPa for both of the tests.

The tests are shown in Figure 4.1-17 and Figure 4.1-19. It is seen, that settlement occurrence, for both tests, due to the compression loading. In Figure 4.1-18 the force-normalized displacement plane is presented. The test is compared at 19000 cycles. The test with frequency of 0.05 Hz shows displacement of 0.73 mm, whereas the test with frequency 0.1 Hz displacement of 1 mm settlement. This indicates that there is small influence in terms of loading frequency, but not significant, as stated also by [4-01].

#### 4.1.6 Observation on stiffness behaviour under vertical cyclic loading

The stiffness coefficient  $k$ , is estimated as the slope between the force and normalized displacement. This is done in order to see if the stiffness of the soil changes during the “lifetime”, or in other words with the number of cycles. This will relate to the design and the dynamic characteristics of the structure. In particular with the first natural frequency of the foundation as this can reach the excitation frequencies. Figure 4.1-20 defines how the stiffness coefficient is obtained. Figure 4.1-21 shows the stiffness coefficient normalized with respect to the 1st value, as defined by Figure 4.1-20. Plotting the normalized stiffness as function of cycles it is easy to see if the stiffness is increasing or decreasing.

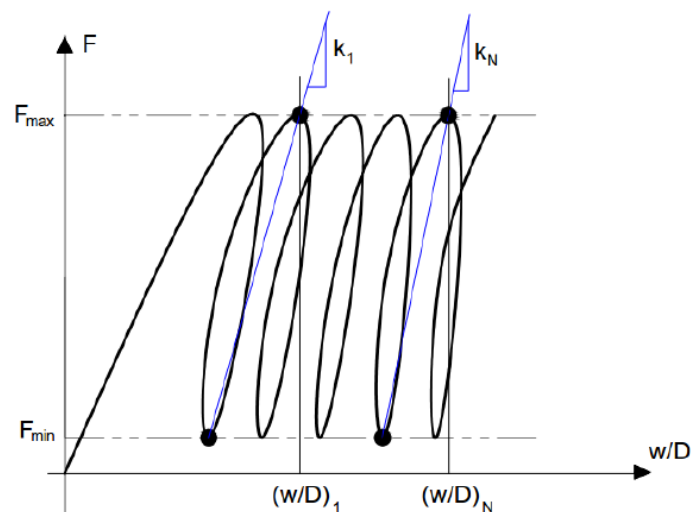


Figure 4.1-20 – Stiffness coefficient estimation and symbol definition, starting from second cycle of the test.

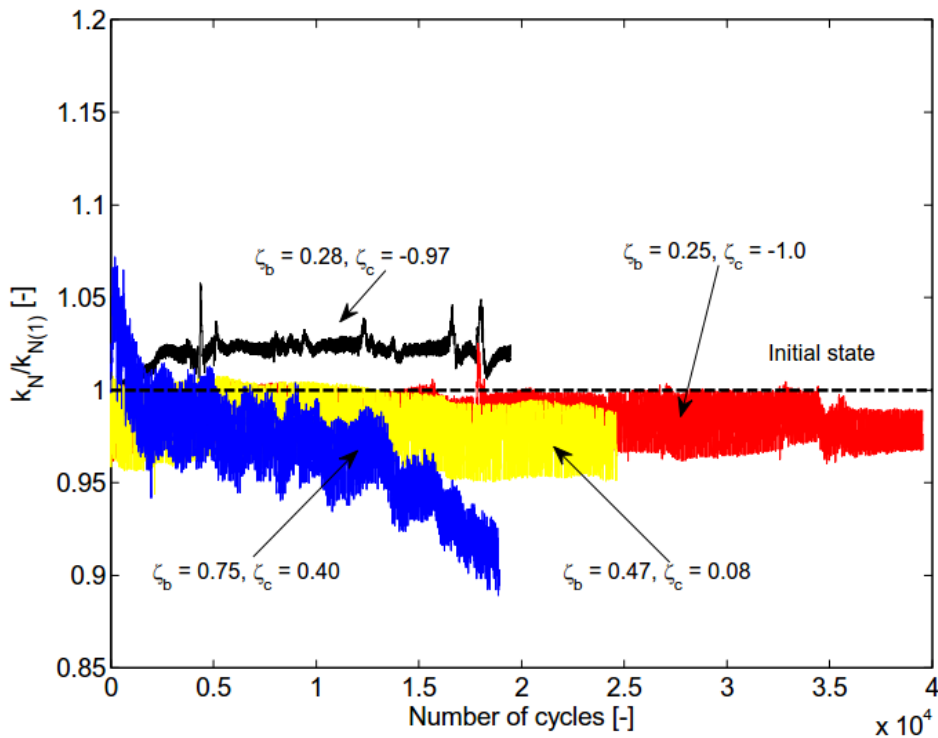


Figure 4.1-21 – Stiffness coefficient change with respect to number of cycles in different regimes. Test No.: 130313 (black), 130314 (red), 130315 (yellow), 130316 (blue).

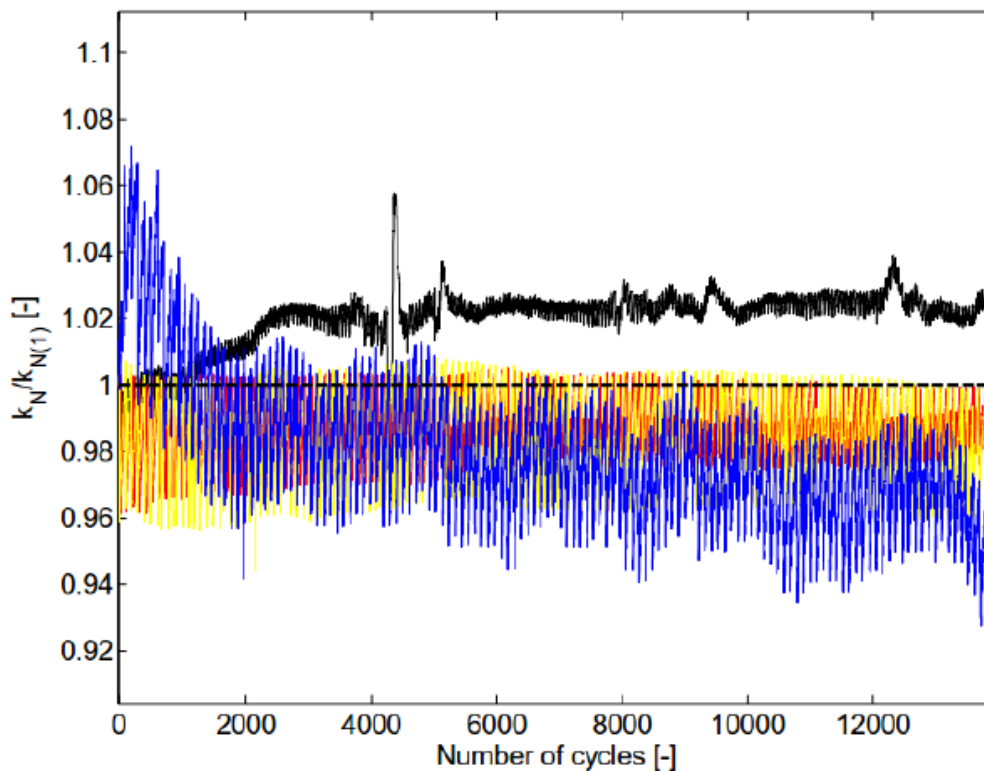
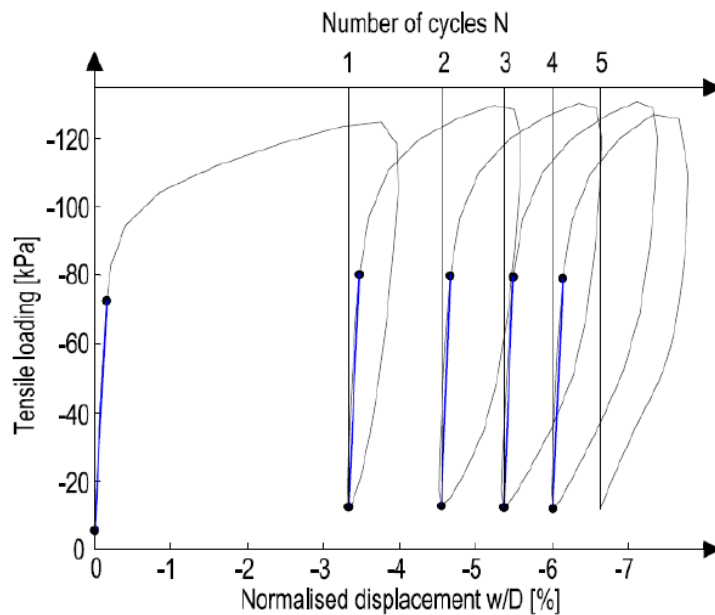


Figure 4.1-22 – Magnified view for the first 10 000 cycles from the stiffness coefficient change. Test No.: 130313. (black), 130314 (red), 130315 (yellow), 130316 (blue).



**Figure 4.1-23 – Defining the loading stiffness coefficient change with respect to number of cycles in pure tension (Test No. 130317).**

As a result, it can be seen in Figure 4.1-21, that test in tension and compression with loading frequency of 0.05 Hz ( $\zeta_b = 0.28$ ,  $\zeta_c = -0.97$ ), shows small increase of stiffness coefficient, whereas the test with similar properties ( $\zeta_b = 0.25$ ,  $\zeta_c = -1.0$ ) and loading frequency 0.1 Hz displays small decrease followed by stable data points. On other hand, two tests only in tensile regime with loading frequency of 0.1 Hz, was observed. Test with  $\zeta_b = 0.47$ ,  $\zeta_c = 0.08$ , have small decrease in stiffness and stabilizing phase until the end. Test with properties  $\zeta_b = 0.75$ ,  $\zeta_c = 0.40$ , shows small increase in the first 2000 cycles followed by decrease in stiffness. One of the tensile loading tests (Test. No.130317) with amplitude of 50% of the reference static load, indicated increase in loading stiffness coefficient.

For better precision Figure 4.1-23 presents the region of the loading part, where the stiffness coefficient was obtained. This path is not tangential or secant slope, but connecting slope between the 1st point of the loading phase and a point on the loading path. This procedure is in a way arbitrary, but gives general overview of the loading stiffness coefficient.

Clearly, it can be said that stiffness increased significantly with only 5 cycles. The loading stiffness coefficient is normalized with the 2nd value of the sequence, as by authors' choice, it was decided to present also the first cycle in order to see the difference of the pattern. With cycle N5, stiffness increased nearly 7 times with respect to the 2nd cycle. This indicates that soil is stiffening up during the performance of this test.

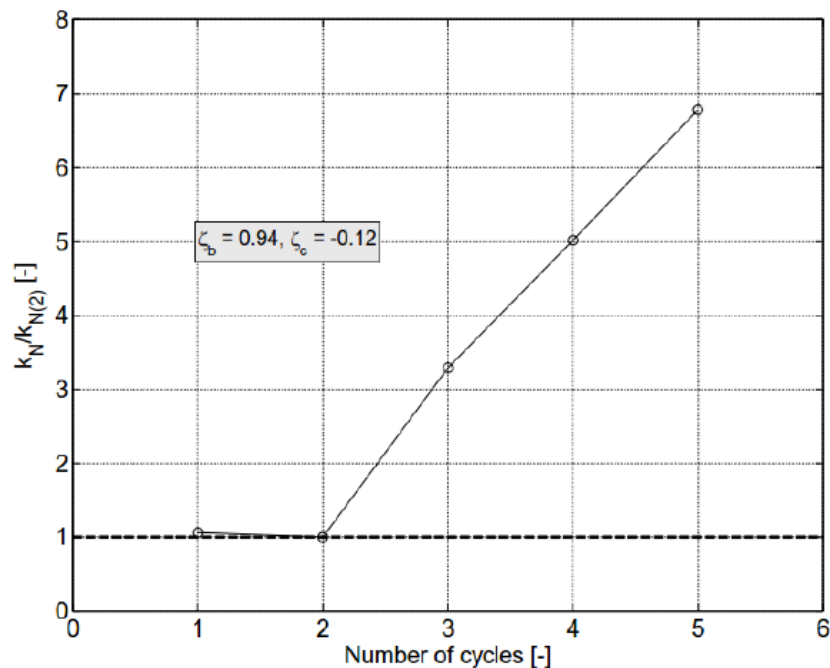


Figure 4.1-24 – Loading stiffness coefficient change with respect to number of cycles in pure tension (Test No. 130317).

#### 4.1.7 Conclusions and recommendations

This sub-section has presented selected results from a series of tests conducted on medium-scale driven bucket foundation subjected to long-term vertically cyclic loading. In some cases, results were presented in dimensionless output with the intention to present the data in a better way for the final evaluation.

Some of the conclusions are based on normalizing the data by itself, in order to observe the behaviour and use the results for comparisons in future tests in similar field. General overviews of different cyclic loading regimes were presented and clear estimation trend was given. Low and high amplitudes behaviour onto the footing were compared and ratios in-between them were assessed. Additionally, the rate of the loading frequency was analysed and as a result it can be concluded that there is insignificant effect over the cyclic performance.

Due to the lack of post-cyclic loading phases, it is difficult to clearly state whether there is a close correlation between monotonic tensile tests and cyclic loading results or not. Nevertheless, from the available post-cyclic tests data, it can be said that the results show similar output.

Based on the amount of presented data in this subsection, it can be concluded that it is possible to decrease the amount of cycles (time of performance during testing) in a significant manner, as e.g. the rate of the footing displacement becomes constant after  $\sim 5000 - 10000$  cycles. More tests have to be performed in order to establish at good correlations between  $\zeta_b$ ,  $\zeta_c$  and the development of permanent deformations. The same is valid concerning the influence on the stiffness coefficient.

## 4.2 Soil pile interaction / axial pile loading

In this sub-chapter the experimental campaign on vibro-driven piles carried out by Fraunhofer IWES in 2015 is described. As in more details explained in [4-02] the main aim of the test campaign is to explore the tensile bearing behavior of vibro-driven piles.

In Section 4.2.1, the facility, the properties of the material used and the foundation specimen are presented. In Section 4.2.2, the investigation techniques adopted to assess the sample properties are described. In Section 4.2.3 all the test and pre-test phases are defined. In Section 4.2.4 example test results are depicted. According to the deliverables description of the project an interpretation of the experimental data by means of empirical numerical models is given in [4-02].

### 4.2.1 Description of testing facility and material

The foundation test pit of the Test Centre for Support Structure in Hannover, Germany, is a 9 m wide, 14 m long and 10 m deep volume contained within reinforced concrete walls. Abutment walls on one side of the pit (also made of reinforced concrete) and various displaceable steel frames, allow for testing offshore wind foundations subjected to different loading conditions. A picture of the empty sand pit is shown in Figure 4.2-1.

The testing material used is uniformly graded siliceous sand called *Rohsand 3152*, which was provided by the company Schlingmeier Quarzsand GmbH & Co. KG based in Schwülper, Germany. The grading curve and some fundamental properties of the sand are presented in Figure 4.2-2 and Table 4.2-1, respectively.

In Table 4.2-1  $e$  is the void ratio,  $G_s$  is the specific gravity,  $C_u$  the uniformity coefficient,  $C_c$  the curvature coefficient and  $d_{60}$  the grain diameter corresponding to 60% passing material by weight.

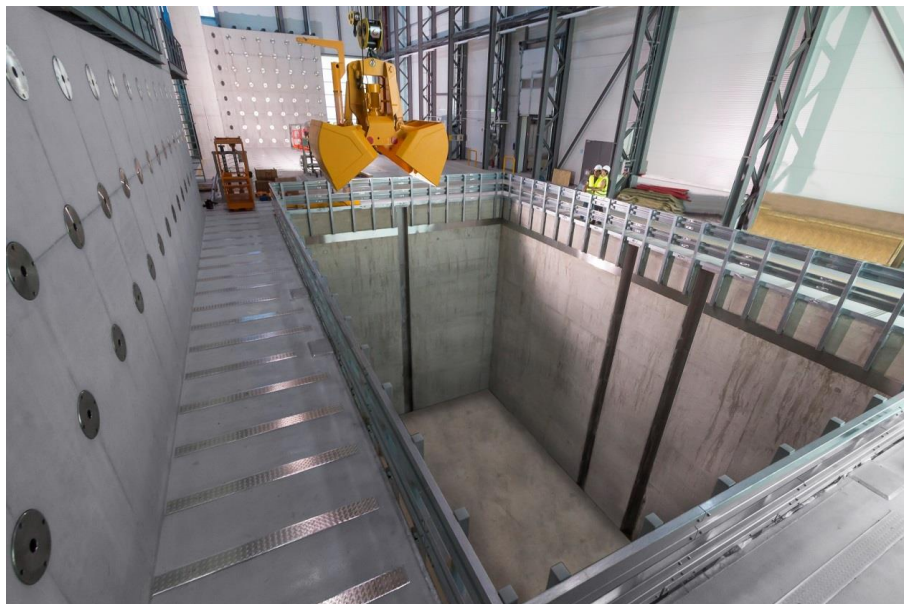


Figure 4.2-1 – Sand pit of Test Centre before sand filling. Dimensions: 9 m x 14 m x 10 m.

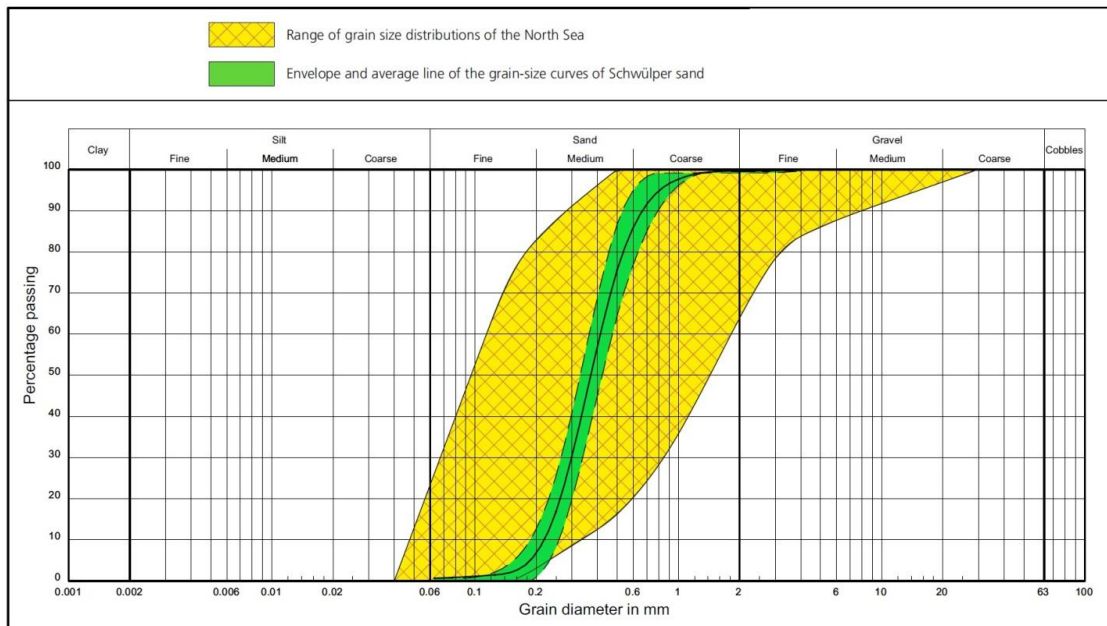


Figure 4.2-2 – Grading curve of *Rohsand 3152* and representative grading curves of well-graded sands in the North Sea.

Table 4.2-1 – Properties of *Rohsand 3152*.

Property	Symbol	Unit	Value
Maximum void ratio	$e_{max}$	-	0.83
Minimum void ratio	$e_{min}$	-	0.44
Specific gravity	$G_s$	-	2.65
Coefficient of uniformity	$C_u$	-	1.97
Coefficient of curvature	$C_c$	-	0.98
Grain diameter to 60% passing material	$d_{60}$	mm	0.407

#### Preparation of the sand sample

High-quality geotechnical experiments require systematic sand preparation procedures to obtain:

- Uniform samples
- Repeatable samples
- A designated degree of compaction.

In the present experimental campaign the aim was to recreate each time medium dense to dense sand condition (relative density,  $D_r$  between 55% and 70%), which is representative for sandy deposits of the North Sea. In order to achieve these, the sand was poured into the pit and compacted in subsequent layers. A photograph showing the sand being poured into the pit is depicted in Figure 4.2-3. The compaction was performed with direction plate compactors (see Figure 4.2-4). The sand layers had a thickness of about 30 cm before the compaction which reduced to 25 cm after the compaction. The first three meters from the bottom were prepared with an initial thickness of 50 cm.



Figure 4.2-3 – Sand pit filling operation.

Water into the test pit was poured from above carefully and slowly during the preparation process. After the compaction of the last layer, the water level was finally adjusted to a depth of 80 cm from the top of the pit.

#### Property of the piles

Two identical piles (Pile 1 and Pile 2), made of steel S355, were installed and subsequently tested. The dimensions of the piles are diameter,  $D = 0.508$  m, length,  $L = 7,5$  m (embedded length  $L_e = 6$  m) and wall thickness,  $t = 6.3$  mm. In order to be able to install and test the pile a flange to which adaptors for installation and tensile test can be adjusted was designed and is depicted in Figure 4.2-5.

#### 4.2.2 Assessment of the sand sample properties

Three soil investigation techniques were adopted to assess the sand status after the soil preparation procedures:

- Soil core sampling
- Dynamic probe light (DPL)
- Cone penetration test (CPT)

In the following the three investigation methods are presented and the results collected are discussed.



**Figure 4.2-4 – Sand compaction of subsequent layers by using direction plate compactors.**

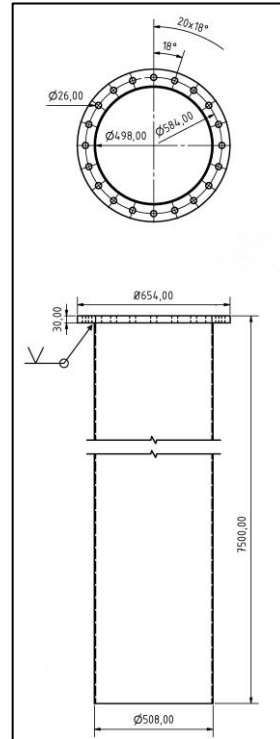


**Figure 4.2-5 – Dimensions of piles and flange.**

### Soil core sampling

The sand pit area was equally divided into six sub-areas. The soil samples were carefully taken with a cylindrical soil sampler (diameter 10 cm, length 12 cm) from every sub-area after each compacted layer. The relative density ( $D_r$ ), averaged over the six sub-areas is plotted against depth in Figure 4.2-6. The relative density ranges between 0.55 and 0.72 with an average value of 0.61. It is worth to mention that the relative density calculated with soil core needs neither empirical parameter nor sophisticated empirical equation to be evaluated, and is therefore highly reliable. Thus, the curve referring to soil core samples depicted in Figure 4.2-6 is utilized further in this section as mean of comparison to validate the empirical methods necessary to evaluate  $D_r$  with DPL and CPT.

Information on the sand pit uniformity can be acquired by plotting the coefficient of variation (COV) of the relative density data of the six samples with depth (see Figure 4.2-7). The COV shows very moderate values, revealing uniform relative density across the sand pit and low variation with depth.

### Dynamic probe light and cone penetration test

To gain more insight into uniformity and to predict parameters of the soil, dynamic probing tests (DPLs) and cone penetration tests (CPTs) were performed. More importantly, CPTs were necessary to be able to use CPT-based methods for axially loaded piles [4-07], as explained [4-02]. In Figure 4.2-8 a plan view of the sand pit with indication of the inspection points (IPs) referring to CPTs and the position of the piles installed, are shown. DPLs and CPTs were performed closed to each other (0.5 m distance) on purpose, to gain a correlation law between the two methods of investigation. DPLs were conducted down until 6 m whereas CPTs down until 9.4 m.

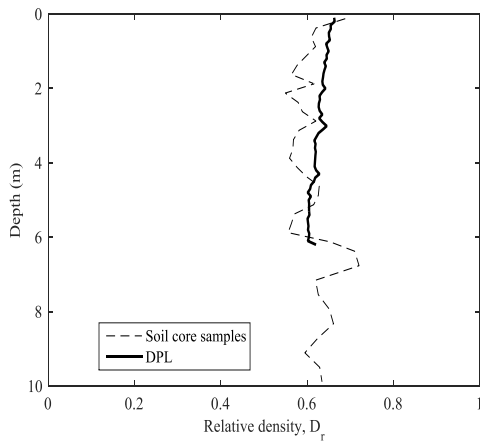


**Figure 4.2-6 – Average relative density calculated over the cross area of the sand pit with soil core samples and dynamic probe light.**

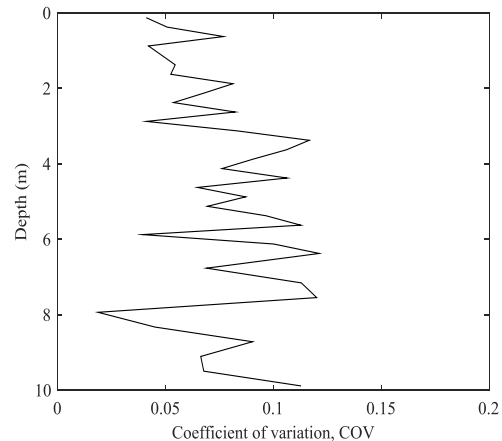


**Figure 4.2-7 – COV of the relative density with depth calculated with soil core samples.**

In Figure 4.2-6 the average relative density over the cross area on the base of DPLs data, calculated according to [4-08], is plotted against depth. The good match with the soil core samples curve is remarkable and corroborates the compaction state found with direct sampling. In Figure 4.2-9 the CPT profiles of all the IPs are depicted. The cone tip resistance ( $q_c$ ), between 1m and 7m of depth, presents values ranging from 5 to 23 MPa. Approximately the last three meter (roughly between 7m and 9.4m),  $q_c$  decreases unexpectedly. This is most probably due to the different preparation system used in that specific region of the sample. It should be noticed though that this inconsistency will not negatively affect the test results. Indeed, the tensile bearing capacity of piles does not involve soil below the pile but almost exclusively soil adjacent to the pile shaft. A peek up to 35 MPa in tip resistance can be seen at a depth of 6.2 m. This occurred in position IP3 where most probably the cone came across a stone.

When interpreting CPT data of real sites, it is common to use relationships correlating CPT tip resistance and relative density of the sand (see [4-09], [4-10], [4-11], [4-12]). These approaches are also used here in an attempt to understand which method is the most suitable given the experimental condition described above. The estimation of  $D_r$  based on the average value of  $q_c$  (across the area of the pit) is plotted against the depth according to four different approaches in Figure 4.2-10.

It must be mentioned that these approaches were thought for real scale data and much larger depth. Their usability in moderate depth (namely 10 m) is not obvious. For the sake of clarity, it is reiterated here that the relative density values found with soil core sampling (Figure 4.2-6) is used in the following as a mean of comparison.

By observing Figure 4.2-10, it is immediately apparent that the four approaches give very different  $D_r$  values, particularly within the first two to three meters. This is not surprising, and can be ascribed to the influence of low confining pressure on the cone resistance [4-12]. However, the four approaches seem to be more consistent to each other with increasing depth, as it was expected. The method [4-12] is clearly the most suitable for the sand pit, at least for the first two to three meters. This is a reassuring observation since this particular method was formulated *ad hoc* for shallow penetration CPTs. From three meter down to seven meter the method overestimates the  $D_r$  by 15%. The methods [4-10] and [4-09] overestimate the  $D_r$  quite remarkably at shallow depth for then being more consistent at six to seven meters depth. The method [4-11] underestimates  $D_r$ , particularly in the first meters. Down at six to seven meters depth [4-11] seems to give very appropriate values of  $D_r$ .

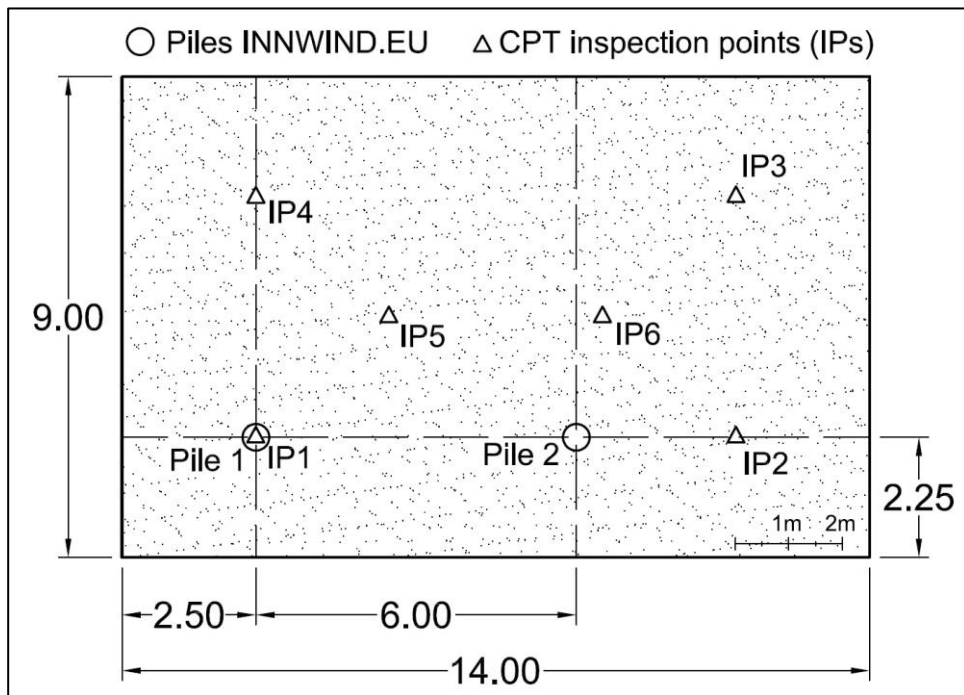


Figure 4.2-8 – Plan view of the sand pit with indication of the inspection points (IPs) for CPT and the piles installed for the INN WIND.EU project.

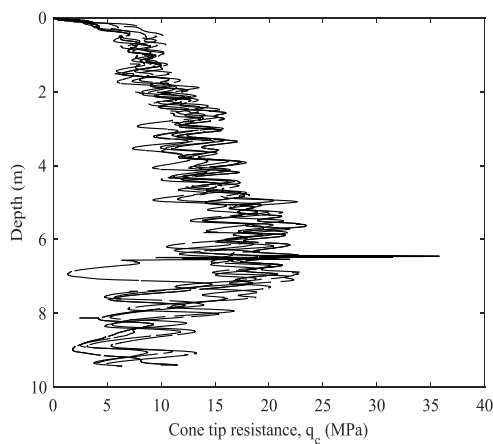


Figure 4.2-9 – CPT profiles of all the inspection points.

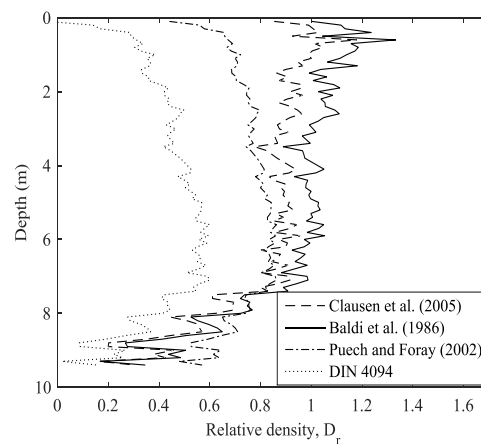


Figure 4.2-10 – Interpretation of CPT data. Relative density according to four different methods.

### Soil properties after the installation of Pile 1

The influence of the vibro-installation of Pile 1 on the soil condition was investigated by means of DPLs. In Figure 4.2-11 the plan view of the geotechnical pit with the DPLs inspection points before (MPvs) and after (MPns) the installation of Pile 1, are displayed. DPLs were performed at 1D, 2D, 3D, 4D, 8D and 12D (MPn1 to MPn6 on Figure 4.2-11) from the position of Pile 1. The results of MPn1, MPn2, MPn3, and MPn5 are shown together with MPv4 in terms of relative density in Figure 4.2-12.

Up to 3D distance from the pile the relative density, averaged over the depth, is between 6% and 12% smaller compared to the undisturbed sample (MPv4). MPn5 (4D distance) present only a 1.5% reduction in  $D_r$ . The DPLs performed after the installation at 8D and 12D (MPn6 and MPn4, respectively) are plotted together with MPv3 in Figure 4.2-13. Similarly to MPn6 in Figure 4.2-12, the tests made after the installation do not present a significant change in relative density (3% looser sand for MPn6 and 4% looser sand for MPn4).

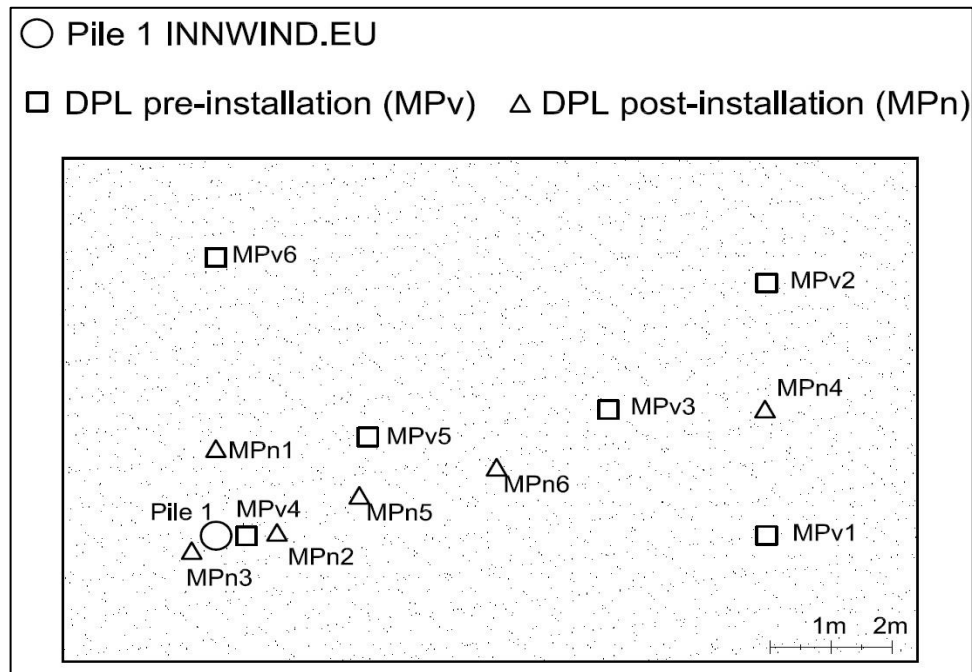


Figure 4.2-11 – Plan view of the sand pit with indication of the DPL inspection points before (MPVs) and after (MPNs) the installation of Pile 1.

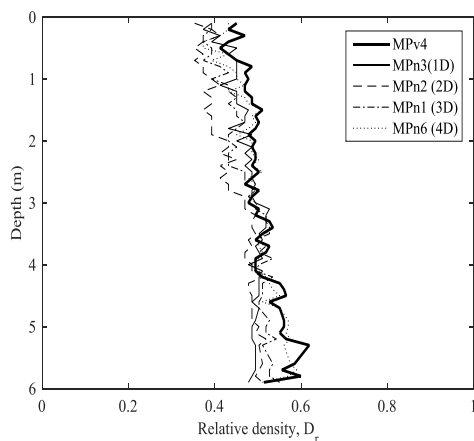


Figure 4.2-12 – DPL results after the vibro-installation. Close to the pile.

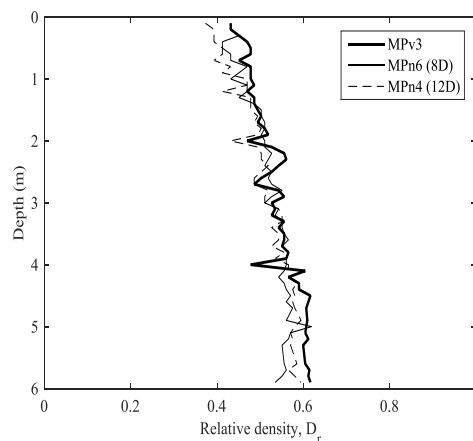


Figure 4.2-13– DPL results after the vibro-installation. Far from the pile.

### 4.2.3 Test phases

In this section, all the steps overtaken before and during the tensile test are described. The two piles installed are named Pile 1 and Pile 2 (see also Figure 4.2-8). Pile 1 was installed first and was subjected to pre-loading before being tested under tensile loading. Pile 2 was installed thereafter and was only subjected to tensile loading until failure. A picture of the test setup with both piles indicated is shown in Figure 4.2-14.

#### Instrumentation of the piles

During the tensile loading tests the piles are monitored with load cell of the actuator, displacement transducer of the actuator and external displacement transducer. The actuator used for the test has a 500 kN capacity. The external displacement transducer was installed in order to enable an objective and system-independent measurement of the pile uplift during tensile loading. The transducer is linear variable displacement transformer (LVDT) of the type WLH 200 from the company MESSTRON, a picture of it is displayed in Figure 4.2-15. The external transducer and the internal transducers of the actuator are connected to an analyzer unit which in turn broadcasts the signal to the computer unit where the data are stored with a sampling frequency of 100 Hz.



Figure 4.2-14 – Picture of the test setup just before the tensile loading test of Pile 2. Both piles for the INN WIND.EU project are depicted.

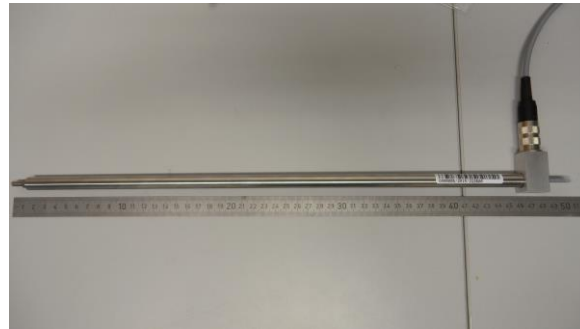


Figure 4.2-15 – Inductive displacement transducer used for external measurement of the displacement during pile uplift.



Figure 4.2-16 – Pile 1 at the beginning of the installation.



Figure 4.2-17 – Pile 1 at the end of the installation.

### Installation of the piles

The installation of the piles was carried through by an external firm specialized in deep foundations. Pile 1 was installed on February 5th 2015. Pile 2 was installed on August 6th, 2015. The installation was performed by an excavator. The vibrator was connected to the arm of the excavator which in turn grabbed the adaptor placed at pile head. Two pictures of Pile 1 at the beginning and at the end of the installation are given in Figure 4.2-16 and Figure 4.2-17.

On the right-hand side the excavator is shown. On the left-hand side of the picture it can be seen the vibrator, type Müller MS-5 HFBV, which grabs the pile head by means of the adaptor flange. The frequency of the vibrator can be up to 45 Hz. The pile penetrated the sand with a velocity of approximately 0.1 m/s. Pile 2 was installed with a vibrator type ICE 8RFB, which has a frequency of up to 14 Hz.

### Pre-loading phase

As already mentioned Pile 1 was subjected to relevant pre-loading before being axially tested in tension. The pre-load applied in this phase consisted of cyclic horizontal load with different frequencies and amplitudes. Additionally, a 0.9 m deep scour was artificially created. In this manner the influence of set-up effect (about 200 days after the installation), scour and pre-loading is to be explored. Given the scale of the system it was not possible to apply the different effects to more than one foundation. As a result of that the implications of these affecting variables could not be possibly decoupled. However, it is well known that the set-up effect is generally beneficial to the bearing behavior of piles as also recently reported by [4-13]. Further, scouring phenomena are doubtlessly negative for the bearing behavior. The question arises as whether pre-loading produces beneficial or detrimental effects on the pile shaft capacity. This query could unfortunately not be answered within this experimental campaign.

### Tensile loading test

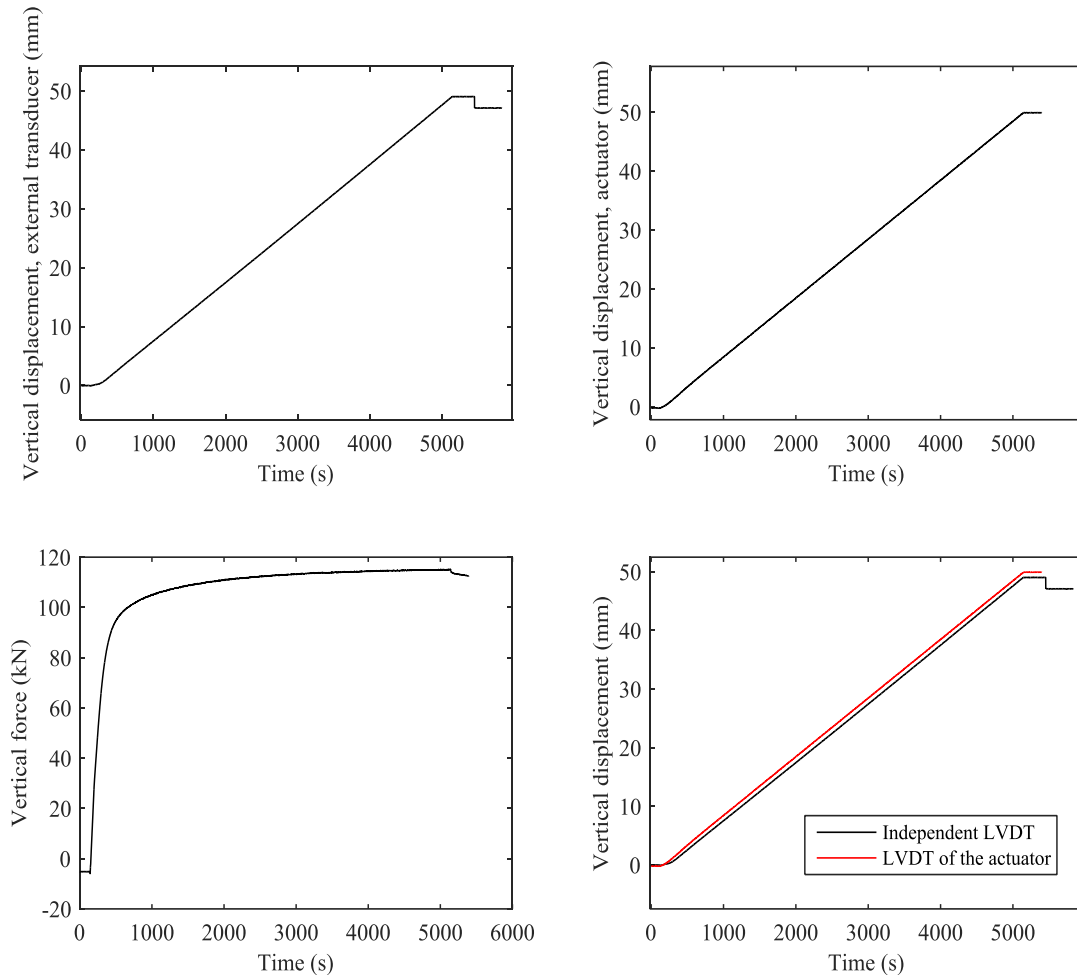
A very robust steel structure formed by two vertical columns and supporting a horizontal beam was employed to offer the necessary counterweight to the system (see Figure 4.2-14). The 500 kN hydraulic cylinder (actuator) was connected to the beam on one side and, by means of a steel adapter plate, to the flange of the pile. A picture of the setup for Pile 2 is illustrated in Figure 4.2-18 where displacement transducer, pile and actuator are indicated. A particular view of the Pile 2 setup depicting the displacement transducer in details is shown in Figure 4.2-19. The test was performed in a displacement-controlled manner. To make sure that no pore pressure building up could possibly occur during the tensile loading test, the displacement rate applied was very low,



Figure 4.2-18– Pile 2 before the tensile loading test.



Figure 4.2-19– Particular of Pile 2 setup, displacement transducer.



**Figure 4.2-20 – Force, displacement of the actuator and independent displacement of the pile during the tensile loading test plotted against time.**

0.01 mm/s. This displacement rate of the actuator was designated and was also confirmed by the external displacement transducer.

Before the tensile loading test a difference of 82 cm between soil in the inside and outside of the pile was measured. After the test the difference between soil in and out was measured again with the same result. This proves that the behavior of the pile was substantially fully plugged during the tensile loading test.

#### 4.2.4 Example results

Relevant measurements of the test performed against time follow below in Figure 4.2-20. In the graph at the top left the external vertical displacement is shown. The curve is linear with a rate of 0.01 mm/s as it was designated. The curve proves that LVDTs can be used successfully in this kind of tests. On the graph at the top right the displacement of the actuator is plotted. The behavior is very similar to the previous graph but a fundamental discrepancy can be noticed in the graph down right where the two curves are plotted together within the same time domain. The important observation revealed by the graph is that the independent LVDT begins later to move

than the displacement transducer of the actuator. This is definitely a reasonable behavior since before the head of the pile (which is measured with the external LVDT) begins its vertical motion the beam supporting the actuator also moved in towards the pile. This is exactly the reason why an external displacement transducer is essential for this kind of tests. On the same graph note also that the reading of the external displacement keeps giving a signal for a while after complete unloading while force and displacement transducer of the actuator stop giving reliable values. This is due to a flaw of the connection between control and measuring system. However this occurs at the end of the test and does not have any consequence on the load-displacement curve recorded. On the graph down left it is seen how the force evolves. Obviously, the curve shows a non-linear behavior since the test was displacement controlled.

Overall, the results outlined and discussed in this section seem to demonstrate that the test preparation and the test itself were successfully performed and can potentially contribute to the research on vibro-driven piles for jacket sub-structures.

### References

- [4-01] Byrne, B. & Houlsby G. (2002). "Experimental Investigations of Response of Suction Caissons to Transient Vertical Loading". Part of the "Journal of Geotechnical and Geoenvironmental Engineering", Vol. 128, No. 11, November 1, 2002. ASCE, ISSN 1090-0241/2002/11-926-939.
- [4-02] INN WIND.EU: Innovations on component level (final report). Deliverable 4.1.3, 2015.
- [4-03] Vaitkunaite, E., Ibsen, L.B., Nielsen, B.N. (2014) "New Medium-Scale Laboratory Testing of Bucket Foundation Capacity in Sand", Proc. of the 24th International Ocean and Polar Engineering Conference, Busan, South Korea. ISBN (electronic) 978-1 880653 91-3.
- [4-04] LeBlanc, C., Byrne, B. W. & Houlsby, G. T. (2010a). "Response of stiff piles to random two-way lateral loading". *Geotechnique*, 60(9), 715-721.
- [4-05] LeBlanc, C., Houlsby, G. T. & Byrne, B. W. (2010b). "Response of stiff piles to random two-way lateral loading". *Geotechnique*, 60(2), 79-90.
- [4-06] Kelly, R. B., Houlsby, G.T. & Byrne, B. W. (2006). "A comparison of field and laboratory tests of caisson foundations in sand and clay". *Geotechnique*, 56(9), 617-626.
- [4-07] API 2011: ISO 19901-4:2003 (Modified), Petroleum and natural gas industries-Specific requirements for offshore structures, Part 4-Geotechnical and Foundation Design Considerations.
- [4-08] EN 1997-2: Eurocode 7: Geotechnical design - Part 2: Ground investigation and testing [Authority: The European Union Per Regulation 305/2011, Directive 98/34/EC, Directive 2004/18/EC], 2007.
- [4-09] Baldi, G., Bellotti, R., Ghionna, V., Jamiolkowski, M., Pasqualini, E.: Interpretation of CPT's and CPTU's. 2nd Part: drained penetration on sands. Proc., 4th Int. Geotech. Seminar: Field Instrumentation and In Situ Measurements, Nanyang Technol. Univ., Singapore, 143-162, 1986.
- [4-10] Clausen, C. J. F., Aas, P. M., Karlsrud, K.: Bearing capacity of driven piles in sand, the NGI approach. - Proc., 1st Int. Symp. on Frontiers in Offshore Geotechnics, Balkema, Perth, Australia, 677-681, 2005.
- [4-11] DIN 4094-1, 2002: Baugrund; Felduntersuchungen. Teil 1: Drucksondierungen. - Beuth, Berlin.
- [4-12] Puech, A. and Foray, P.: Refined model for interpreting shallow penetration CPTs in sands. - Offshore technology conference (OTC 14275). Houston, Texas, 2002.
- [4-13] Lehane B.M., Schneider J.A. and Xu X: A review of design methods for offshore driven piles in siliceous sand. UWA Report GEO 05358.

## 5 CONCLUSIONS

To reduce the cost of offshore wind energy, innovative solutions for the sub-components of the support structure are necessary. This document reports four experimental campaigns focused on different elements of the sub-structure. The test campaigns are thoroughly described and some example results are illustrated.

Sandwich tubes for the braces of jacket structures were tested under combined axial (N) and moment (M) loading. Three different eccentricities were tested. The load-deflection graphs indicate that a nearly linear increase of load is followed by an abrupt reduction of capacity until finally reaching a residual load. From the load-deflection curves of the non-eccentric tests a relation between loading rate and specimen stiffness could be observed. Interestingly, strain gauges measurements reveal that when the load is not eccentric, the vertical deformation spreads evenly over the annulus area until 60% of the maximum load. As expected, the ultimate axial load decreases with increasing eccentricity. An interaction diagram in terms of M and N is proposed at the end of the sub-chapter.

Eleven tests were performed on sandwich tubes for joints. Force and shear stresses in the adhesive were measured. In all cases failure occurs for complete delamination as a result of a fracture on the bonding line of the inner pile. Relevant difference between failure in tension and compression were found and therefore more research on finding adequate bonding material should be pursued.

It is worth to emphasize that the main advantage of the contributions on soil-foundation interaction is that both bucket foundations and vibro-driven piles are tested in medium-scale (1:5 – 1:10). Clearly, this gives realistic results and avoids the great problems related to scaling of non-cohesive materials like sand. Post-cyclic monotonic curves of bucket foundations reveal a capacity which is rather similar to the pure monotonic one. Besides, the loading frequency seems not to influence the cyclic performance.

The specimen preparation for the vibro-driven pile test shows that the soil is uniformly compacted. The compaction degree attained is between medium-dense and dense. The two methods used to estimate the compaction degree agree to each other to a large extend. The soil condition was checked also after the vibro-pile installation. A slightly higher compaction degree was found within a distance of 3-4 pile diameters from the middle of the pile. The main plots of the pile tested clearly show that the test was successfully accomplished.